Ab-initio study of electronic and transport properties of single- and co-doped silicon nanostructures

by

Le The Anh

submitted to
Japan Advanced Institute of Science and Technology
in partial fulfillment of the requirements
for the degree of
Doctor of Philosophy

Supervisor: Professor Hiroshi Mizuta

School of Materials Science
Japan Advanced Institute of Science and Technology

December, 2014

Ab-initio study of electronic and transport properties of single- and co-doped silicon nanostructures

Mizuta Lab, 1140210, Le The Anh

Abstract

Keywords: binding energy, density functional theory, non-equilibrium Green's function, single-doped silicon nanostructures, co-doped silicon nanostructures.

Recently, single dopant electronics has opened a new group of extremely-small and low power devices, including single-electron FETs. The basic operations of single dopant devices are based on single-electron tunneling mediated by a single dopant. The binding energy of donor electrons should be much higher than the thermal energy to ensure single dopant devices operate at room temperature; therefore, it is important to accurately estimate the binding energy of donor electrons not only for single dopant devices in particular, but also for nanometer-scale devices in general. In bulk silicon, the donor ground state is shallow and independent from the bottom of the conduction band of Si crystal. In nano silicon, which has dimensions smaller than the Bohr radius of donor electrons in bulk, the interaction between the donor related states and the host Si conduction states becomes significant due to the strong nanoscale confinement. The binding energy in nano Si therefore should be studied from a different point of view to the binding energy in bulk Si.

By performing DFT calculations, I have determined the binding energy of electrons bound to a single phosphorus donor atom in silicon nanorods. The projected density of states (PDOS) and 3D wavefunctions (3DWFs) analysis can clarify the gradually decreasing contribution of the phosphorus electron states from the donor ground states to the higher energy donor excited states due to the hybridization of the donor electron states and silicon electron states. Therefore, I can identify the energy of the first conductive state. The binding energy of the donor electrons in the single P-doped Si nanorods, which have an average radius smaller than 1.4 nm (which is smaller than a_0 = 3nm, the Bohr radius for phosphorus electrons in bulk Si) is calculated as the difference between the first conductive state and the donor ground state. I have found that the binding energy is still around 1.5 eV. As the size decreases below 1.4 nm, the first conductive state is capped near the top of the atomistic effective potential at the phosphorus donor site, whereas above the potential top the electron wavefunctions are more delocalized and can attribute to conduction. This causes the binding energy in sub-1.4 nm Si nanorods to be weakly dependent on the sizes. This fact signifies the good tolerance level of the binding energy, which governs the operating temperature of single dopant-based transistors in practice. The transmission spectra calculated by the non-equilibrium Green's function, which reflects into the transport properties of electrons in silicon nanorod devices, show consistent results with the PDOS-3DWFs method, proving the validity of the new method.

Following this, I have applied the PDOS-3DWFs method to investigate the dependence of binding energy on the position of P atoms in single P-doped cross-shaped Si nanotructures. When the P atom is located at the wing of the cross-shaped nano structure, it is more difficult for the wavefunction to spread entirely within the structure, especially along the horizontal transport direction; this results in higher binding energy for the P atom at the wing of the cross-shaped Si nanostructure. The experimental study of stub-channel FETs, which is similar to cross-shaped model established by the Tabe group from Shizuoka University, shows that electron tunneling has higher barrier energy than conventional straight shape FETs. The theoretical results of the cross-shaped Si nanostructures are consistent with the experimental results for the stub-channel FETs.

Finally, the interaction between donor D^0 and acceptor A^0 ground states have been investigated theoretically in phosphorus-boron co-doped silicon nanorods; the different effective atomistic potential at the P site and B site decreases from about 1.5 eV to around 0.5 eV when the two dopants move closer towards each other from 2.17 nm to 0.23 nm. This suggests that the built-in atomistic potential in co-doped silicon nanorods strongly depends on the P-B separation. Moreover, the D^0 wavefunction is destructive at the boron site, whereas the A^0 wavefunction is destructive at the phosphorus site. When two dopants come closer, the overlapping of the B and P original atomic orbitals increases. As a result, the values of wavefunctions of A^0 and D^0 at the boron and phosphorus sites decrease. The wavefunctions become less localized and shallower, which is consistent with the transmission analysis that transmissions associated with dopant induced states change in nature from discrete to continuous.

Acknowledgments

First of all, I would like to thank Prof. Hiroshi Mizuta of Japan Advanced Institute of Science and Technology (JAIST) for his supervision and his kind support for my study at JAIST. He was always ready to discuss with me even in his hectic schedule. I have learnt a lot not only in doing a research but also in life from his valuable discussion.

I wish to express my sincere gratitude to Prof. Michiharu Tabe of Shizuoka University for his kind financial support and discussion. He always encouraged me and gave me a complete freedom to persue the research. I also would like to thank Dr. Daniel Moraru and colleagues in Tabe Lab. Their experimental studies motivated me to do this research.

I want to take this opportunity to thank the members of dissertation committee: Prof. Hiroshi Mizuta, Prof. Hideyuki Murata, Prof. Goro Mizutani, Assoc. Prof. Mikio Koyano, and Prof. Michiharu Tabe for generously offering their time, support, guidance and good will throughout the preparation and review of this document.

It is an honor for me to thank Dr. Muruganathan Manoharan in Mizuta Lab for his valuable discussion and support. I would like to thank all of my friends for the their encouragement and their support in living life.

I would like to express my deepest gratitude and great thanks to my family for their supporting and encouraging.

Contents

Chapter 1

Introduction

1.1 Miniaturization of Si devices

The International Technology Roadmap for Semiconductors (ITRS) 2013 forecasts that the MOSFET will become a sub-10 nm device after 2020, when its physical gate length reaches 9 nm (Fig. 1.1). State-of-the-art MOSFETs in 65 nm technology nodes (2007) featuring a physical gate length of 25 nm with conventional architecture have been demonstrated in a research environment. As the CMOS scaling continues to reduce the feature size, variability will become a major issue among other problems as identified in the ITRS; there are various different sources of variability in current silicon device/process technologies such as ultrathin SOI MOSFET channel thickness fluctuation and lithography-defined gate pattern size fluctuation. These are called line-edge roughness fluctuations and they produce a quantitative measure of the roughness along the side edges of lithographically printed patterns [1, 2, 3]. In state-of-the-art silicon CMOS technology (16/14 nm technology nodes), the line-edge roughness fluctuation is not negligible.

The most critical variability however is the potential fluctuation induced by dopant atoms, which are completely randomly distributed in the Si substrate and heavily-doped sources and drain regions as illustrated in the insets to Fig. 1.1. The variation in the number and position of dopant atoms in the active region makes each MOSFET microscopically different and has already caused significant variations from device to device. The variations in dopant statistics will have a fatal impact on the functionality, yield, and reliability of the corresponding circuits and systems at a time when the fluctuation margins shrink due to continuous reduction

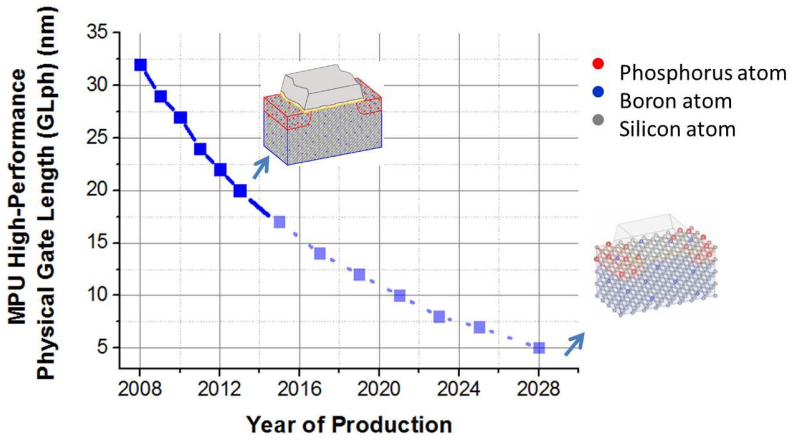

Figure 1.1: CMOS miniaturization trend targets from the International Technology Roadmap for Semiconductors with schematic MOSFET images (Source: http://www.itrs.net/Links/2013ITRS/).

in supply voltage and an increased transistor count per chip. The CMOS scaling theory [5] argues that the channel doping concentration in scaled MOSFETs should be high enough to suppress the impact of drain-to-channel capacitive coupling on the energy barrier height from the source to the channel. As a result, considering the volume of the channel region and the doping concentration of the sub-32 nm planar bulk MOSFETs [6], one can conclude that the average number of impurities in planar bulk MOSFETs approaches a few ten of dopant atoms.

1.2 Random dopant fluctuations

A number of theoretical and experimental studies have discussed the impacts of random dopant fluctuations on the significant variations in the threshold voltage and drive current of MOSFETs [7, 8, 9]. In their 3-D atomistic simulation studies, A. Asenov and his colleagues [8, 9] showed that threshold voltage fluctuations are determined not only by the fluctuation in the dopant number but also in the individual dopant position. Figure 1.2 shows the potential distributions at the Si/SiO_2 interface of two microscopically different MOSFET's, both with 170 dopant atoms in the channel depletion region. The upper device in figure 1.2 has a threshold voltage of 0.78 V, while the lower device in figure 1.2(b) has a threshold voltage of 0.56 V. In the upper device, six to seven dopants in the middle of the channel almost equally spaced along the channel width block the current path and are responsible for the high threshold voltage. In the lower device on

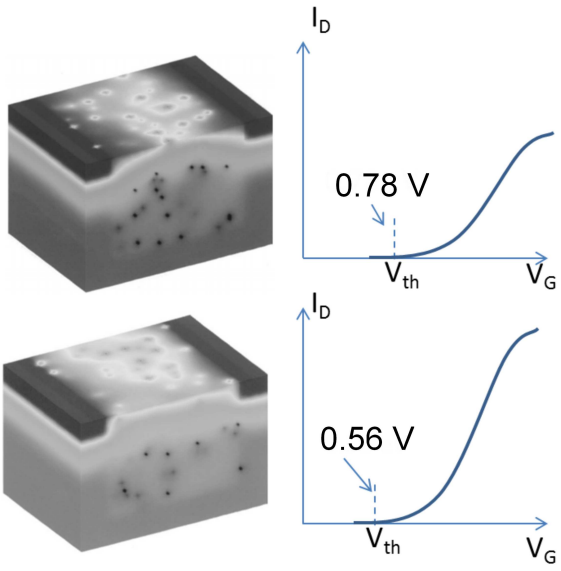

Figure 1.2: Potential distributions at the Si/SiO_2 interface of two microscopically different MOSFETs both with 170 dopant atoms in the channel depletion region. Upper: MOSFET with threshold voltage 0.78 V; Lower: MOSFET with threshold voltage 0.56 V. After [9] .

the other hand there is virtually no dopant at the surface, resulting in a low local threshold voltage. This study demonstrates that random dopant fluctuations are an increasingly significant factor in sub-100 nm CMOS technology.

Hiramoto and his colleagues also experimentally studied the impact of SOI thickness fluctuations on threshold voltage (V_{th}) variation in ultra-thin body SOI MOSFETs [10] confirming that V_{th} variation drastically increases as the SOI thickness of the channel region is thinned down to 3 nm. Figure 1.3 shows the V_{th} shift increase in the SOI thickness below 3 nm in detail in [10].

In order to improve the uniformity of the dopant distributions and well control the dopant positions, some techniques have been developed for deterministic doping. Shinada and his colleagues used the developed single-ion implantation technique, which enables them to implant dopant ions one-by-one into a fine semiconductor region until the desired number is reached. Figure 1.4shows the schematic picture of a Single-ion implantation system, while the following demonstrates the atomic force microscope (AFM) image of etch-pits created in a fission track detector by single ions. There are an average of three P ions in a pitch of 100x100 nm with lateral precision of about 50 nm. Another technique that allows matter to be controlled at the atomic scale is the scanning tunneling microscope

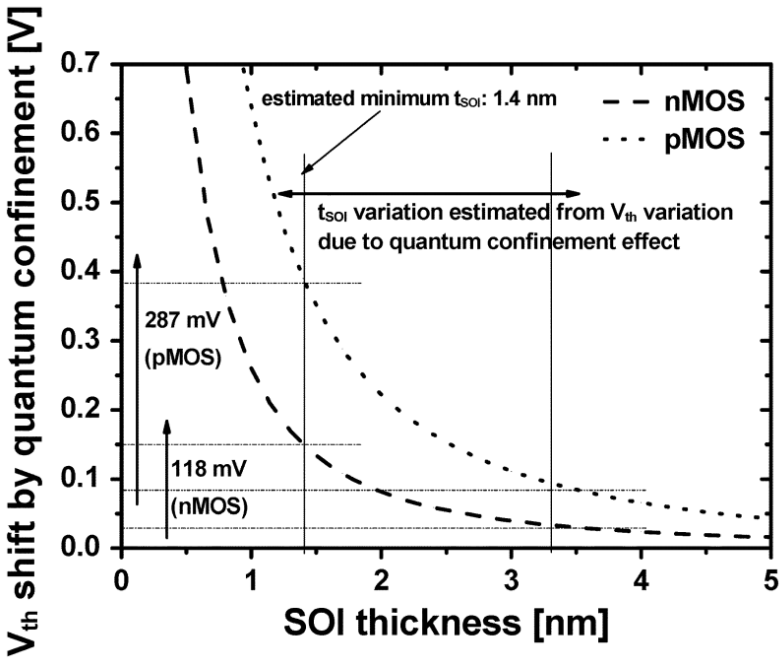

Figure 1.3: Calculated threshold voltage shift by the quantum confinement effect. Only the lowest energy level is taken into account. After [10].

[12], which can manipulate individual atoms and molecules on surfaces. Figure 1.4 shows the schematic picture of a scanning tunneling microscope atomic manipulation; there is an average of one P atom included in a 3-Si-dimers area and the lateral precision is about +/- 3.8 Å. These two techniques have made significant efforts to control single dopants but the fact is that they are still the state-of-the-art-technology and are still far from industrial fabrication.

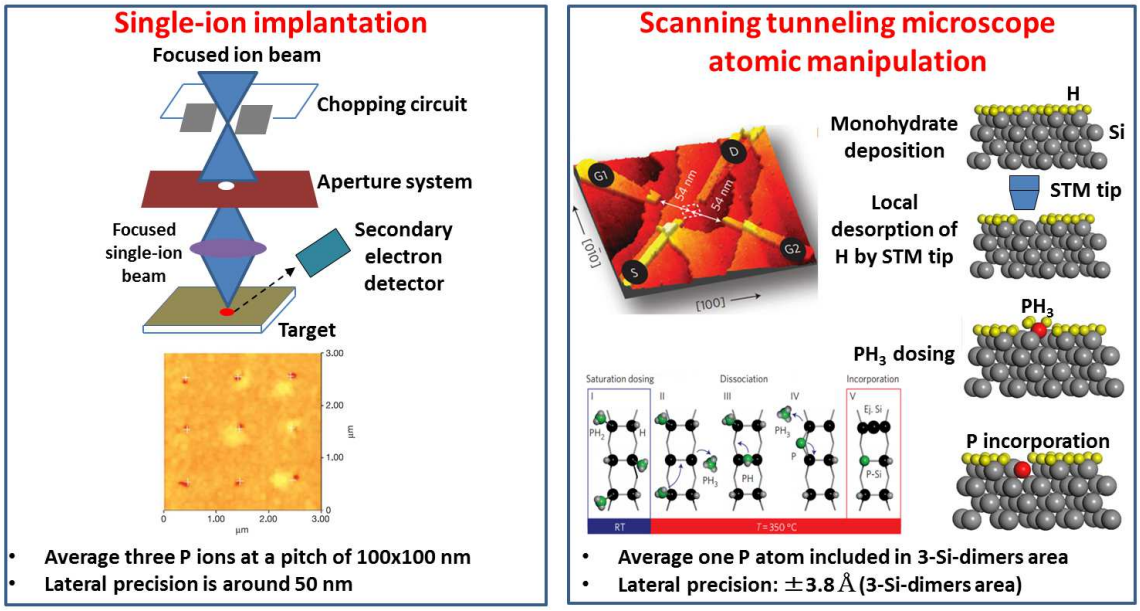

Figure 1.4: left: the schematic picture of a Single-ion implanation system, right: the schematic picture of a scanning tunneling microscope atomic manipulation. The microscope pictures were taken from Ref. [11, 12].

1.3 Single dopant electronics

Although the single-ion implantation technique and the scanning tunneling microscope technique allow us to well control the positions of the dopants, these techniques are still the state-of-the-art-technology and are still far from industrial fabrication. On the other hand, in parallel simple technological progress offers the possibility of utilizing individual dopant atoms to realize novel functional devices at the nanometer scale [13, 14] to make devices in practice. One of the basic operations of these nanometer-scale devices is based on single-electron tunneling mediated by a single dopant. First, let me briefly discuss single electron transistors (SET) and silicon single electron transistors. The first SET was proposed by Averin and Likharev in 1986 [15], , and the first experimental work was demonstrated by Fulton and Dolan in 1987 at Bell Laboratories [16]. The SET consists of two electrodes known as the drain and the source, connected through tunnel junctions to one common electrode with a low self-capacitance known as the island. The electrical potential of the island can be tuned by a third electrode, known as the gate, capacitively coupled with the island. In the blocking state no accessible energy levels are within the tunneling range of the electron on the source contact, and all energy levels on island electrodes with lower energies are occupied. When a positive voltage is applied to the gate electrode the energy levels of the island electrodes are lowered. The electron can tunnel into the island, occupying a previously vacant energy level. From there it can tunnel into the drain electrode where it inelastically scatters and reaches the drain electrode. SETs have been used to measure quantum bit [17], to calculate the local chemical potential in semiconductor systems [18], , to characterize and operate single electron pumps and traps [19], , and for macroscopic charge quantization [20]. Silicon based Single Electron Devices (SEDs) have attracted significant attention because of their higher operating temperature and larger potential for circuit applications with a clear emphasis on silicon-on-insulator (SOI) substrates [21, 22].

Single electron transport through one or several dopant atoms in low-doped channels of FETs has been characterized both experimentally [23, 24, 25] and theoretically [26, 27, 28]. These single-dopant devices have been considered as the building blocks for applications such as quantum computing [29, 30], single electron transfer [31, 32], and single-dopant ionization detection [33]. Recent progress in dopant engineering [34] and dopant mapping techniques [35, 36] is promising in terms of improving our understanding of single-dopant devices.

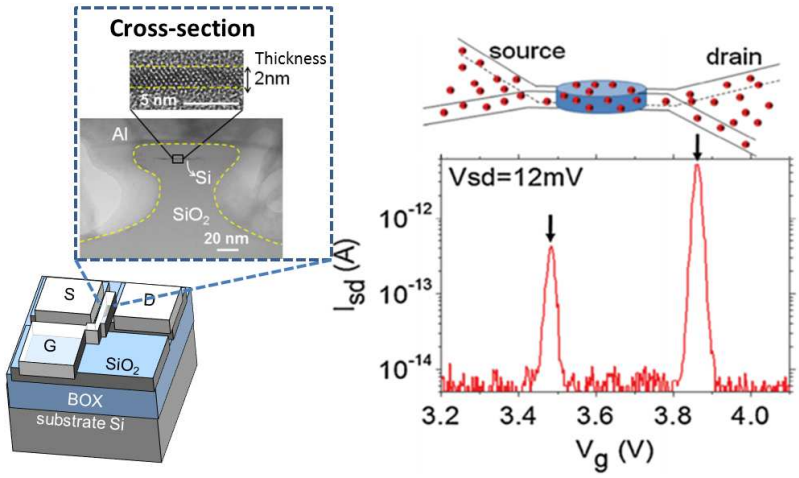

Figure 1.5: Left: Schematic structure of the ultra thin disk-shaped-channel FET and the TEM cross-section image. Right: The $I_{sd} - V_g$ characteristics of untral thin disk-shaped-channel FET. Arrows indicate two smooth peaks originated from single electron transport through single dopants. After [37].

The operation of single-dopant devices is based on single-electron tunneling mediated by a single dopant. These individual dopants can be accessed even in dopant-rich environments, where the channel contains more than one isolated dopant atom. In Physical Review Letters [37] the Tabe group from Shizuoka University reported that single-electron transport through a single dopant can be achieved even in a random background of many dopants without any precise placement of individual dopants. Figure 1.5 shows the $I_{sd} - V_g$ characteristics of randomly doped devices at 17 K; they exhibit single-peak features for the first observable current peaks, which is a signature of the creation of a single quantum dot in the channel, and two observed peaks arise due to single-electron transport through different single-dopant quantum dots. Due to quantum confinement effect, a high barrier energy for electron tunneling via single dopants and therefore a high operation temperature close to room temperature can be achieved.

The fact that single dopants can be accessed electrically even in dopant-rich environments offers the opportunity to develop applications based on dopant arrays. The Tabe group showed that dopant-based single-electron turnstiles can be achieved and tuned with a combination of two gates [31, 38]. Moreover, a new memory device concept based on the interaction between dopants has also been developed [39]; they demonstrated that with one donor as a sensor (conduction path) and another donor as a memory node (trap), a system could be used for memory in which sensing is done by a single-electron tunneling current via one

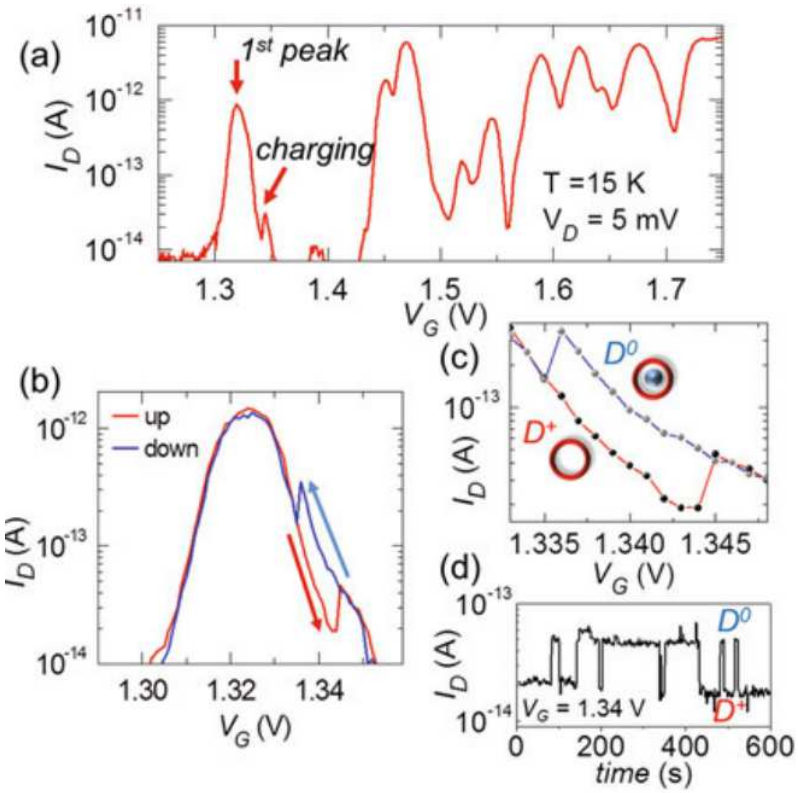

Figure 1.6: Single-electron transfer between two donors. (a) Low temperature $I_D - V_G$ charateristics showing a single-donor current peak used as a sensor for detecting charging and discharging of a neighboring donor. (b)-(c) Charging and discharging are sensed as abrupt jumps of the current and (d) as RTS in the time-domain measurements. After [38].

donor atom while storage is ensured by an individual donor working as a memory node [38, 39, 40]. They measured $I_D - V_G$ characteristics by up-ramping and consecutively down-ramping V_G around the first peak , as shown in figure 1.6. Furthermore, they indentified abrupt current jumps reflecting sudden charges in potential due to a charging or discharging event; thus, they identified devices in which two donors work as a sensor and as a memory node, respectively.

Another application for donor-based systems relies on the interaction between photons and dopants. It has been determined that quantum dot (QD) arrays may work as a building block for single-photon detection, and the Tabe group showed that QD arrays can be replaced by an array of donors [38]. They measured the low-temperature (15 K) $I_D - V_G$ characteristics, as shown in figure 1.7, under conditions if visible light illumination (λ = 550 nm) with low incident flux. The characteristics exhibit irregular current peaks similar to front-gate devices. They also found that RTS characteristics under light illumination are different compared to those evi-

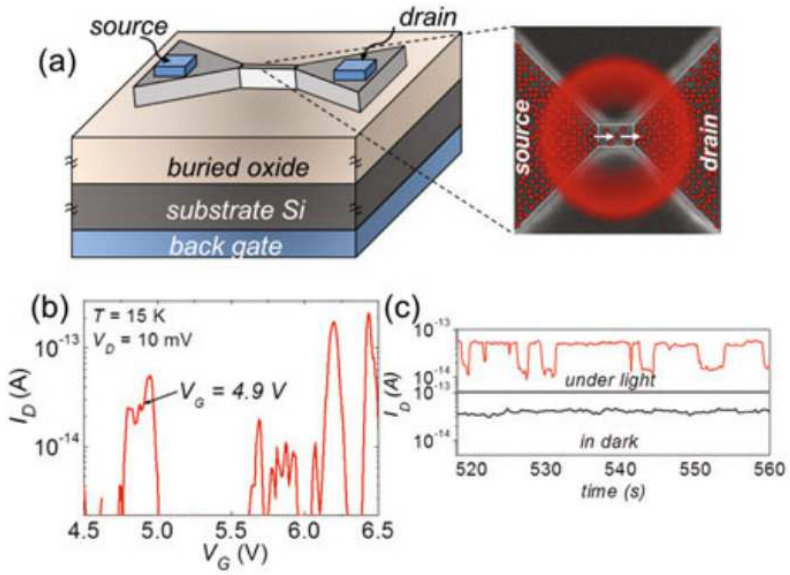

Figure 1.7: Photon-generated electron trapping in donor arrays (a) Device structure of a back-gate SOI-FET for light illumination measurements. With V_G set on the first observable current peak (b), effect of photon absorption in the nanoscale channel can be observed as RTS in the time-domain measurements (c). After [38].

dent under dark conditions, proving that photon-induced carriers remain trapped in the channel for a sufficient amount of time. RTS has mainly two levels, which suggests that only one trap is responsible for the observed current switching. Based on such interactions, dopant-based optoelectronic devices could be developed [38, 40, 41]. Single dopant electronics opens a new group of extremely small and low power devices, including single-electron FETs, single electron memory, single electron transfer devices, and photonic devices.

1.4 Purpose of this study

The basic operations of single dopant devices are based on single-electron tunneling mediated by a single dopant. The binding energy of donor electrons should be much higher than the thermal energy to ensure the operation of the single dopant devices at room temperature, therefore it is important to accurately estimate the binding energy of donor electrons not only for single dopant devices in particular but also for nanometer-scale devices in general. In bulk silicon, the donor ground state is shallow and independent from the bottom of the conduction band of Si crystal, whereas in nano silicon, which has dimensions below the Bohr radius of

donor electrons in bulk, the interaction between the donor related states and host Si conduction states becomes significant due to the strong nanoscale confinement. The binding energy in nano Si therefore should be studied from a different point of view to the binding energy in bulk Si. By performing projected density of state (PDOS) and 3D wavefunctions (3D-WFs) analysis, in this study I have calculated the binding energy of P donor electrons in single P-doped Si nanorod models.

Moreover, nanoscale p-n junctions have not received as much attention as transistors from the point of view of transport via the individuality of dopants. Due to the importance of p-n junctions as building blocks of complex electronic devices, specific study must be dedicated to these structures in terms of the impact of individual dopants on their behavior [42]. Although a theoretical study on the electronic and transport properties of nanoscale p-n junctions in terms of the impact of individual dopants on these properties is required, such a study has not been reported in the past. In this study, I perform first-principle calculations to investigate the electronic and transport properties of phosphorus and boron co-doped silicon nanostructures.

1.5 Organization of this dissertation

This thesis consists of six chapters. The content of the thesis is as follows:

Chapter 1: **Introduction.**I first explain miniaturization in silicon technology and the issue of random dopant fluctuation. Techniques for improving the uniformity of dopant distributions and the position controllability of single dopants are discussed. Following this I introduce single dopant electronics, which offers the possibility of utilizing individual dopant atoms in positive ways. Finally, the purpose of this study is discussed.

Chapter 2: **Methodology.**In this chapter, I summarize the fundamental calculation methods used in this study. Density functional theory (DFT) has been used for the electronic calculation, while the non-equilibrium Green's function (NEGF) is used for the transport calculation.

Chapter 3: **Binding energy of electrons bounded to a single phosphorus donor atom in silicon nanorods.** In this chapter, the binding energy of the phosphorus donor electrons in the single phosphorus-doped silicon nanorods will be calculated using projected density of states (PDOS) and 3D wavefunctions

(3DWFs) analysis. The results will be compared with the results from the conventional method. The origins of the different results from the PDOS-3DWFs method and the conventional method will be discussed.

Chapter 4: **Single phosphorus-doped cross-shaped silicon nanostructures.** I discuss how to estimate the binding energy of phosphorus electrons in single phosphorus-doped cross-shaped silicon nanostructure models by using the PDOS-3DWFs method, as mentioned in Chapter 3. The correlation between my calculations and the experimental study of Si nano stub-shaped transistors will be discussed.

Chapter 5: **Phosphorus-boron co-doped silicon nanostructures.** In this chapter, I perform DFT and NEGF calculations to investigate the electronic and transport properties of phosphorus-boron co-doped silicon nanostructures.

Chapter 6: **Conclusion and future work.**

Chapter 2

Methodology of theoretical study

Recently, numerical simulations have been widely used to provide important information of the electronic and transport properties of materials. In this part of the thesis, I summarize the fundamental theory of the methods used in this simulation studies.

2.1 Ab-initio calculation

2.1.1 Born-Oppenheimer approximation

The aim of ab-initio calculations is to obtain properties of materials from simulations without using any experimental data. First, the Born-Oppenheimer approximation is introduced as the begining of the simulations. Let us assume that we have M nuclei with N electrons. The spin (σ) and position ($\vec{r}$) coordinates of all electrons are:

$(\vec{r_1}, \sigma_1, \vec{r_2}, \sigma_2, ..., \vec{r_N}, \sigma_N) \equiv (\vec{x_1}, \vec{x_2}, ..., \vec{x_N}) \equiv \vec{x}$

The spin (Σ) and position ($\vec{R}$) coordinates of all nuclei are:

$(\vec{R_1}, \Sigma_1, \vec{R_2}, \Sigma_2, ..., \vec{R_N}, \Sigma_N) \equiv (\vec{X_1}, \vec{X_2}, ..., \vec{X_N}) \equiv \vec{X}$

The wavefunction of our system is: $\Psi = \Psi(\vec{X}, \vec{x})$ The Schrodinger equation takes the form:

$$\widehat{H}\Psi = (\widehat{H}_{k,n} + \widehat{H}_{k,e} + \widehat{H}_{p,e-e} + \widehat{H}_{p,n-e} + \widehat{H}_{p,n-n})\Psi(\vec{X}, \vec{x}) = E \cdot \Psi(\vec{X}, \vec{x}) \qquad (2.1)$$

where the $\widehat{H}_{k,n}$ and $\widehat{H}_{k,e}$ are kinetic energies of nuclei and electrons, respectively. The $\widehat{H}_{p,e-e}$, $\widehat{H}_{p,n-e}$, $\widehat{H}_{p,n-n}$ are electron-electron potentials, nucleus-electron potentials, and nucleus-nucleus potentials, respectively. The uncertainty principle gives:

$$\Delta x \cdot \Delta p = \Delta x \cdot m\Delta v \geq \hbar \tag{2.2}$$

$$\Delta X \cdot \Delta P = \Delta X \cdot M\Delta V \geq \hbar \tag{2.3}$$

The first equation is for electron. The second one is for nuleus. The mass of a nulei is thousands times larger than that of an electron. Furthermore, the average kinetic energy equals $3/2kT$. Hence, we have:

$$\frac{\Delta X \cdot \Delta V}{\Delta x \cdot \Delta v} = \frac{m}{M} \ll 1 \tag{2.4}$$

and

$$< \frac{1}{2}MV^2 >=< \frac{1}{2}mv^2 >= \frac{3}{2}kT. \tag{2.5}$$

We simply set:

$$\Delta V =< V^2 >^{1/2} \tag{2.6}$$

$$\Delta v =< v^2 >^{1/2} \tag{2.7}$$

Then, we can obtain:

$$\frac{\Delta V}{\Delta v} \simeq \sqrt{\frac{m}{M}} \ll 1 \tag{2.8}$$

$$\frac{\Delta X}{\Delta x} \simeq \sqrt{\frac{m}{M}} \ll 1 \tag{2.9}$$

Equation 2.8 and 2.9 mean the nuclei move much more slowly and are much more localized in space than the electrons . Hence, we can write:

$$\Psi(\vec{X}, \vec{x}) = \Psi_n(\vec{X}) \cdot \Psi_e(\vec{X}, \vec{x}) \tag{2.10}$$

Equation 2.10 comprises the Born-Oppenheimer approximation. We have separated the motion of nuclei and the motion of electrons in BO approximation, but the *Schrödinger* equation still remains very complicated. For many years, many efforts have been done for solving this equation approximately. The first important

evolution is Hatree-Fock approximation. Based on Hatree-Fock approximation, many advanced approaches have been proposed, for instance configuration interaction (CI), Mϕller-Plesset pertubation theory (MP2, MP4, etc), coupled cluster methods (CC), etc.

2.1.2 Hatree-Fock method

In Hatree-Fock (HF) approximation the many body wavafunctions are built from single particle wavefunctions in the form of Slater determinant.

$$\Psi(\mathbf{x}_1, \mathbf{x}_2, \ldots, \mathbf{x}_N) = \frac{1}{\sqrt{N!}} \begin{vmatrix} \chi_1(\mathbf{x}_1) & \chi_2(\mathbf{x}_1) & \cdots & \chi_N(\mathbf{x}_1) \\ \chi_1(\mathbf{x}_2) & \chi_2(\mathbf{x}_2) & \cdots & \chi_N(\mathbf{x}_2) \\ \vdots & \vdots & & \vdots \\ \chi_1(\mathbf{x}_N) & \chi_2(\mathbf{x}_N) & \cdots & \chi_N(\mathbf{x}_N) \end{vmatrix} \tag{2.11}$$

where χ_i is a single-electron wavefunction and x_i is the general coordinates (includes spin coorinates) of an electron. Minimizing the expectation value of Hamiltonian with respect to single-particle wavefunction χ_i by Lagrange method, one obtains Hatree-Fock equation

$$\widehat{F}\chi_i(x) = \varepsilon_i \chi_i(x) \tag{2.12}$$

where

$$\widehat{F} = \widehat{h_1} + \sum_{j=1}^{N} (\widehat{g_j} - \widehat{k_j}) \tag{2.13}$$

is Fock operator. The Coulomb ($\widehat{g_j}$) and exchange ($\widehat{k_j}$) operators are defined as:

$$\widehat{g_j}\chi_i(x_2) = [\int \chi_j^*(x_1) \frac{1}{r_{12}} \chi_j(x_1)]\chi_i(x_2) \tag{2.14}$$

$$\widehat{k_j}\chi_i(x_2) = [\int \chi_j^*(x_1) \frac{1}{r_{12}} \chi_i(x_1)]\chi_j(x_2) \tag{2.15}$$

It is obvious that in HF approximation one replaces the complex Schrodinger equation by set HF equations for each particle through the introduction of Coulomb and exchange operator. In other words we can say that in HF approximation the complex many particles problem by one particle in the average field of other reaming particles. Since Fock operator depends on the wavefunction that it acts

on, we must solve HF equation iteratively. We start from a set of guessed single particle wavefunction to determine Fock operator, then we solve HF equations to obtain new set of single particle wavefunctions. This procedure is iterated until the convergence criterion is achieved.

Solving 2.12 requires not only the real constants ε_i but also each of orbitals $\chi_(i)$ in every single point i. Roothaan suggested that instead of varying all orbitals in all points, only a finite variation was considered. This was made possible by expanding the orbitals in a set of fixed basis functions:

$$\Psi_l(\vec{x}) = \sum_{p=1}^{N_b} \chi_p(\vec{x}) c_{pl} \tag{2.16}$$

where the basis function χ as well as their number N_b have been chosen in advance and only the expansion coefficients c_{pl} (whose number is finite) are varied. According to the variational method:

$$\frac{\partial F}{\partial c_{pl}} = \frac{\partial F}{\partial c^*_{pl}} = 0 \tag{2.17}$$

HF equation now becomes:

$$\sum_{p=1}^{N_b} [\langle \chi_p \mid \widehat{h}_1 \mid \chi_m \rangle + \sum_{i=1}^{N} \sum_{n,q=1}^{N_b} c_{ni} c^*_{qi} (\langle \chi_p \chi_q \mid \widehat{h}_2 \mid \chi_m \chi_n \rangle - \langle \chi_q \chi_p \mid \widehat{h}_2 \mid \chi_m \chi_n \rangle)] c_{ml} = \varepsilon_l \sum_{m=1}^{N_b} \langle \chi_p \mid \chi_m \rangle c_{ml} \tag{2.18}$$

This is the Hartree-Fock-Roothaan equation that have made HF calculations so widely used. From one set of solution (c_{ml}), one can obtains a matrix eigenvalue equation:

$$Fc_l = \varepsilon_l O c_l \tag{2.19}$$

where $F \equiv (F_{pm})_{N_b N_b}; O \equiv (O_{pm})_{N_b N_b}; c_l \equiv (c_l)_{N_b 1}; O_{pm} \equiv \langle \chi_p \mid \chi_m \rangle c_{ml}$

Solving this equation, we obtain a new set of solution (c_{ml}) and so on until the procedure converges.

2.1.3 Density functional theory

Density functional theory

Parallel to HF methods, different line of electronic structure theory, density functional theory (DFT), was marked by L. H. Thomas and E. Fermi (1927-1928) [43]. Although their approach does not give good result, it introduced an important idea that the energy can in fact be written in term of electronic density. The most important development of DFT was introduced in 1964 by Hohenberg and Kohn [44]. In this work, Hohenberg and Kohn proved two theorems that form a solid mathematical ground for DFT.

Theorem 1: *The external potential is uniquely determined. except for a constant, by the ground state electronic density.*

Since the ground state electronic density uniquely determines v_{ext}, it also determines the Hamiltonian. It hence determines the ground state wavefunction by solving the full many body *Schrödinger* equation. Ground state electronic density, therefore, determines all properties of the system.

Theorem 2: *A **universal functional** for the energy $E[\rho]$ in term of electronic density can be defined, valid for any external potential v_{ext}. For any particular v_{ext}, the exact ground state energy of the system is the global minimum value of this functional, and the density $\rho(r)$ that minimizes the functional is the exact ground state density*

Thus, the complicated full many body problem now can be replaced by a variational problem of minimizing the energy functional $E[\rho]$ with respect to electronics density. However, not all electronic density can be put into the functional $E[\rho]$ for the variation. We can only use the densities that are associated with a certain external potential v_{ext} in this minimization. These densities are so-called v_{ext}*-representable*. And it raises the question of how such electrnic density can be recognized.

Kohn-Sham method

In order to put DFT in practice, Kohn and Sham [45] introduced the concept of non-interacting reference system that have the same density with the real system.

This system is described by the Hamiltonian

$$\widehat{H}_R = \sum_{i=1}^{N}[-\frac{1}{2}\nabla_i^2 + v_R(r_i)] \tag{2.20}$$

where N is number of electrons. The reference potential, $v_R(r_i)$, is defined so that the ground state density of $\widehat{H}_R$ equals to the density of the interest system. Since the Hamiltonian has no electron-electron interactions, its ground state wavefunction can be expressed in the form of Slater determinants as shown in Eq. 2.11. The Density can be written as

$$\rho(r) = \sum_{i=1}^{N} \mid \chi_i(r) \mid^2, \tag{2.21}$$

and the kinetic energy can be approximated as

$$T_R[\rho] = -\frac{1}{2}\sum_{i=1}^{N}\langle\chi_i \mid \nabla^2\chi_i\rangle \tag{2.22}$$

The single-particle orbitals, $\chi_i(x)$, are the N lowest-energy eigenfunctions of one electron Hamiltonian

$$\widehat{H}_R = -\frac{1}{2}\nabla^2 + v_R(r) \tag{2.23}$$

We can now write the energy density functional as follows:

$$E_{KS} = -\frac{1}{2}\sum_{i=1}^{N_{occ}}\langle\chi_i \mid \nabla^2\chi_i\rangle + \int \rho(r)v_{ext}(r)dr + \frac{1}{2}\iint \frac{\rho(r)\rho(r')}{\mid r - r' \mid}drdr' + E_{XC}[\rho]. \tag{2.24}$$

The exchange-correlation functional, $E_{XC}[\rho]$, includes the exchange-correlation effect and the difference of real kinetic energy, $T[\rho]$, and reference kinetic energy, $T_R[\rho]$. By using Lagrange method with the constraint of the orthonormalization of the single-particle wavefunction, $\chi_i(r)$, to minimize the energy functional with respect to the single-particle wavefunction, we obtain Kohn-Sham equation

$$[\frac{1}{2}\nabla^2 + v_{eff}(r)]\chi_i = \varepsilon_i\chi_i \tag{2.25}$$

where effictive potential, $v_{eff}(r)$, is defined as

$$v_{eff} = v_{ext} + \int \frac{\rho(r))}{\mid r - r' \mid}dr + v_{XC} \tag{2.26}$$

The exchange-correlation potential, v_{XC}, is the functional derivetives of the exchange-correlation functional with respect to ρ

$$v_{XC} = \frac{\delta E_{XC}}{\delta \rho} \tag{2.27}$$

Since efective potential, Eq. 2.26, depends on the density, we need to solve it iteratively. We start from a set of guess single-particle wavefunction to calculate the density. From this density we next calculate effective potential, and the solve Kohn-Shame equation, Eq. 2.25 to get a new set of single-particle wavefunction. The procedure will stop, if the convergence criterion is achieved. If the convergence criterion is not achieved, then we start again with this set of single-particle wavefunction.

Exchange-correlation functionl

In Khon-Sham formalism, most of the contributions to the electronic energy of an interested system can be treated exactly. All unknown parts are now put in to the exchange-correlation functional V_{XC}, which include non-classical portion of electron-electron interaction and the component of the kinetic energy not covered by the non-interacting reference system. The quality of the DFT approach is mainly determined by the accuracy of the chosen approximation to V_{XC}. Unlike conventional wave function based methods, in DFT there is no systematic way towards improved approximate functionals. It is very important to carefully study the performance of particular functional with respect to a suitable set of reference data.

2.2 Electronic transport calculation

In this section, I present some fundamentals of electronic transport in mesoscopic systems. The main results are refereed from the paper of Wingreen [46] and the book of Datta [47].

2.2.1 Transverse modes

There are analogous to the transverse modes of electromagnetic waveguides. In narrow conductors, the different transverse modes are well seperated in energy and such conductors are often called electron waveguides. We consider a rectangular conductor that is uniform in the x-direction and has some transverse confining potential U(y). The motion of electrons in such a conductor is described by the effective mass equation:

$$[E_s + \frac{h^2k^2}{2m} + \frac{{p_y}^2}{2m} + 1/2m\omega^2y^2]\chi(y) = E\chi(y) \tag{2.28}$$

where $\chi(y)$ is the transverse function. The eigenenergies and eigenfunctions are given by: $\chi_{n,k}(y) = u_n(q)$ where $q = \sqrt{m\omega_0/h}y$

$$E(n,k) = E_s + \frac{h^2k^2}{2m} + (n + 1/2)h\omega_0 \tag{2.29}$$

The dispersion relation is sketched in Fig. States with different index n are said to belong to different subbands just like the subbands that arise from the confinement in the z-direction. The subbands are often referred to as transverse modes in analogy with the modes of an electromagnetic waveguide.

2.2.2 The current and conductance

To calculate the current we note that the states in the narrow conductor belong to different transverse modes or subbands. Each mode has a dispersion relation E(N,k) with a cut-off energy $\epsilon_N = E(N, k = 0)$ below which it cannot propagate. The number of transverse modes at an energy E is obtained by counting the number of modes having cut-off energies smaller than E:

$$M(E) = \sum_N \theta(E - \epsilon_N) \tag{2.30}$$

The current is given by

$$I = \frac{2e}{h}\int_{-\text{inf}}^{+\text{inf}} f(E)M(E)dE \tag{2.31}$$

The conductance of large samples obeys an ohmic scaling law: $G = \sigma W/L$. But as we go to smaller dimensions there are two corrections to this law. Firstly there is

an interface resistance independent of the length L of the sample. Secondly the conductance does not decrease linearly with the width W. Instead it depends on the number of transverse modes in the conductor and goes down in discrete steps. The Landauer formula incorporates both of these features:

$$G = \frac{2e^2}{h}MT \tag{2.32}$$

The factor T represents the average probability that an electron injected at one end of the conductor will transmit to the other end. If the transmission probability is unity, we recover the correct expression for the resistance of a ballistic conductor including the contact resistance. We could view the Landauer formula as a mesoscopic version of the Einstein relation:

$$\sigma = e^2 N_s D <-> G = \frac{2e^2}{h}MT \tag{2.33}$$

with the conductivity replaced by the conductance, the density of states replaced by the number of transverse modes (or subbands) and the diffusion constant replaced by the transmission probability.

2.2.3 Non-equilibrium Green's function method

A system including a central scattering region connected by two lead is considered. The Hamiltonian for this system can be expressed as:

$$H = H_{ll} + H_{rr} + H_C + H_{C,ll} + H_{C,rr} \tag{2.34}$$

where H_{ll}, and H_{rr} are the Hamiltonian of the left and right lead, respectively. The Hamiltonian of the central region:

$$H_C = \sum_n (\epsilon_n + qU_n) d_n^+ d_n \tag{2.35}$$

The term U_n is the self-consistent Coulomb potential of the central region. The couplings between the central region and the left and right leads are described by the term $H_{C,ll}$ and $H_{C,rr}$. Theoretically, the Hamiltonian, H, of the system must be calculated seft-consistently. When H is determined, the current flow through the system is also determined. The steady current can be written as: where H_{ll} and H_{rr} are the Hamiltonian of the left and right lead, respectively. The Hamiltonian

of the central region:

$$I = I_{ll} = I_{rr} = \frac{q}{h} \int d\epsilon [f(\epsilon - \mu_L) - f(\epsilon - \mu_R)] T(\epsilon) \tag{2.36}$$

where, $T(\epsilon)$, is the transmission coefficient. It can be expressed as:

$$T(\epsilon) = Tr[\gamma_L(\epsilon - qv_L)] G^r(\epsilon) \gamma_R(\epsilon - qv_R)] G^a(\epsilon)] \tag{2.37}$$

Here, G^r and G^a are the retarded and advanced Green's function of the central region. A central results of the NEGF method is that the density matrix of the central region under non-equilibrium conditions, ρ, is given by:

$$\rho = -\frac{i}{2\pi} \int G^<(\epsilon) d\epsilon \tag{2.38}$$

where $G<(\epsilon)$ is calculated using the Keldysh equations:

$$G<(\epsilon) = Gr(\epsilon) \sum (\epsilon) Ga(\epsilon) \tag{2.39}$$

and

$$\sum (\epsilon) = i\gamma_L(\epsilon - qv_L) f_\alpha(\epsilon - \mu_L) + i\gamma_R(\epsilon - qv_R) f_\alpha(\epsilon - \mu_R) \tag{2.40}$$

The advantage of the NEGF method is that it includes all information of the non-equilibrium quantum effects and the non-preiodic boundary conditions.

2.2.4 Combination of DFT and NEGF calculations

The DFT method can take into account the many-body interaction effects, while the NEGF method can treat the non-equilibrium effects and the non-preiodic boundary conditions. The combination of the DFT and the NEGF methods, therefore, allows us to calculate electronic transport properties of open systems accurately. In this research, all first-principles calculations were performed using the software OpenMX, which is implimented both the DFT and the NEGF methods. In particular, the first-principles calculations were performed using the code OpenMX, which is based on density functional theories (DFT) [44, 45], norm-conserving pseudopotentials [48, 49, 50, 51, 52], and pseudoatomic localized basis functions [53]. All calculations are performed by using generalized gradient approximation (GGA) PBE version of the exchange-correlation potential [54]. The convergence

threshold for the self-consistent field (SCF) iteration is 10^{-6} Hartree. The pseudo-atomic orbitals are used as basis functions to expand one-particle Kohn-Sham wave functions. The cut-off radius of the basis functions is 7.0 . Due to the large-scale calculation, only s-, p-, and d-state radical functions are used to represent the basis functions of Si, P, H, and Au. The k grid 1x2x3 is used for the SCF calculation. For the isolated Si nanorods, we use the conventional diagonalization method in the SCF iterations. For the Si nanorods sandwiched by two semi-infinite Au electrodes, we use the non-equilibrium Green's function (NEGF) method within the collinear DFT [55], which is implemented in the OpenMX code in the SCF iteration. The NEGF method enables us to calculate the transmission spectra of electrons through the Si nanorods from the left to the right lead.

Chapter 3

Binding energy of electrons bounded to a single phosphorus donor atom in silicon nanorods

3.1 Introduction

The technological progress offers the possibility of utilizing individual dopant atoms to realize novel functional devices at the nanometer scale [13, 14]. One of the basic operations of these nanometer-scale devices is based on single-electron tunneling mediated by a single dopant [37]. The binding energy of donor electrons should be much higher than the thermal energy to ensure the operation of single dopant devices at room temperature [13].; therefore, it is important to accurately estimate the binding energy of donor electrons not only for single dopant devices in particular but also for nanometer-scale devices in general. In past studies, the binding energy of dopant electrons has been defined as the difference between the ionization energy calculated for single phosphorus-doped (P-doped) silicon nanostructures and the electron affinity calculated for un-doped silicon nanostructures [56, 57, 58, 59, 60, 61]. This definition has been frequently used in many calculations, from tight binding calculations to full DFT real-space calculations [56, 57, 58, 59, 60, 61]. The first conductive state was determined through the electron affinity of the un-doped silicon nanostructures, thus this conventional definition is similar to the definition of binding energy in bulk silicon. In bulk silicon, the donor ground state is shallow and independent from the bottom of the

Si crystal conduction band. In nano silicon, which has dimensions below the Bohr radius of donor electron in bulk, the interaction between the donor related states and host Si conduction states becomes significant due to the strong nanoscale confinement. The binding energy in nano Si should therefore be studied from a different perspective to the binding energy in bulk Si. The conventional definition however fails to include the strong interaction of electrons at excited states and phosphorus ions, which can be described by the hybridization of donor electron states and silicon electron states in extremely downscaled silicon nanostructures. This hybridization undoubtedly takes a predominant role in the electronic and transport properties of nanometer-scale devices, along with the quantum confinement [62, 56] and dielectric confinement effects [57]. In this study, binding energy is investigated at nanoscale for the first time, which considers the hybridization of the phosphorus donor electron states and silicon electron states explicitly. By utilizing the DFT total energy calculation, the binding energy of the P donor electrons in the single P-doped Si nanorods from the projected density of state (PDOS) and 3D wavefunctions (3D-WFs) analysis can be calculated. Finally, I have conducted the transport calculation for the single P-doped Si nanorod connected to the source and drain electrodes. This study has been published in the Journal of Applied Physics **116** (6) 063705 (2014).

3.2 Structures of the single phosphorus doped silicon nanorods

The Si nanorods used in this study are built with the < 100 >orientation along the Z direction and are covered with H atoms in order to passivate all of the dangling bonds. To investigate the effects of quantum confinement on the electronic properties of the nanorods, I built five Si nanorods $Si_{12}H_{28}P$, $Si_{61}H_{75}P$, $Si_{167}H_{147}P$, $Si_{357}H_{243}P$, and $Si_{652}H_{364}P$ - with different sizes. The shapes of the five nanorods are analogous. In all these structures, I consider the P atom to be at the center substitutional site. Table I shows the dimensions of five Si nanorods along the X, Y, and Z axes. I have labeled the five Si nanorods $Si_{12}H_{28}P$, $Si_{61}H_{75}P$, $Si_{167}H_{147}P$, $Si_{357}H_{243}P$, and $Si_{652}H_{364}P$ as SNR-A, SNR-B, SNR-C, SNR-D, and SNR-E, respectively. The average radius $R_{avg} = ((R_x + Ry + Rz)/3)$ is also reported in table I. Figure 3.1(a) shows the views of SNR-B ($Si_{61}H_{75}P$) on the XY and XZ planes.The five SNRs have been embedded in large supercells in order to prevent interactions between the

periodic replicas (about 20 Å of vacuum separates neighboring clusters in the X, Y, and Z directions). To build single P-doped Si nanorods with two electrodes, I used two semi-infinite Au nanowires as the left and right leads, as shown in Fig. 3.1(b). The channels are SNRs. The channels are SNRs. Due to the large scale calculation, the number of Au atoms in each lead has been optimized as 20. The distance between the lead interfaces and the nanorods is about 1.5 Å. The Z < 100 > direction is set as the transport direction from the left lead to the right lead. To minimize the hybridization between the states from two electrodes and the states of the nanorods, fully hydrogen terminated Si nanorods have been used.

Table 3.1: The dimensions of five Si nanorods labeled from SNR-A to SNR-E

Structure	R_x (nm)	R_y (nm)	R_z (nm)	R_{avg} (nm)
SNR-A ($Si_{12}H_{28}P$)	0.356	0.221	0.491	0.356
SNR-B ($Si_{61}H_{75}P$)	0.627	0.352	0.898	0.627
SNR-C ($Si_{167}H_{147}P$)	0.898	0.496	1.304	0.898
SNR-D ($Si_{357}H_{243}P$)	1.069	0.638	1.718	1.069
SNR-E ($Si_{652}H_{364}P$)	1.441	0.767	2.146	1.441

3.3 The hybridization of the phosphorus electron states and silicon electron states

It is well known that, in an un-doped Si nanostructure, the lowest unoccupied orbital degenerates into three groups: one A_1 state, one threefold T_2 state, and one twofold E state [62, 60]. The A_1 orbital has s-like symmetry at its nanostructure center, while the T_2 and E orbitals have a node at the center. The inter-valley couplings split these states. According to the tight binding calculation, the splittings in spherical un-doped Si quantumdot range from 0.1 meV for diameters of 10.32 nm up to 68 meV for diameters of 1.85 nm. As for the P-doped Si nanostructures, I have calculated the splittings of the A_1, T_2, and E states in SNR-B with an average diameter of 1.25 nm. Figure 3.2 shows the projected density of states onto the P donor, with Gaussian broadening of 0.15 eV and Kohn-Sham energy levels from

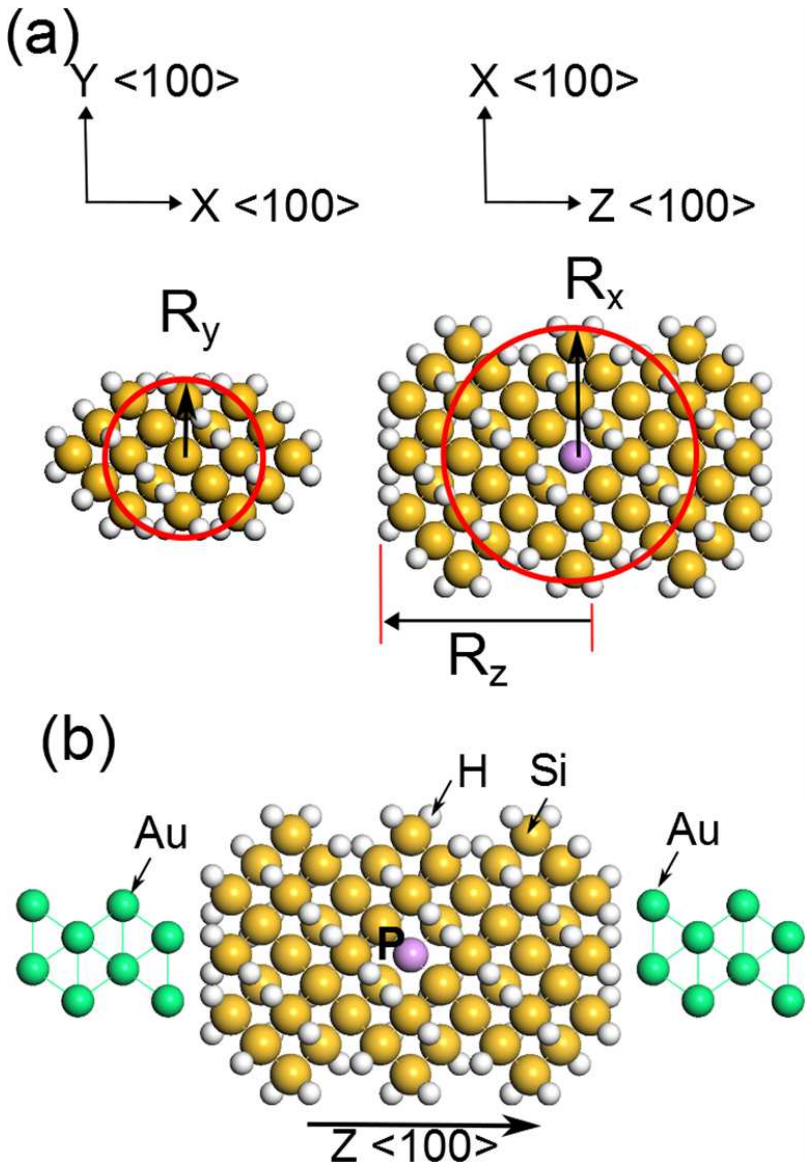

Figure 3.1: (a) The single P-doped Si nanorod SNR-B ($Si_{61}H_{75}P$) viewed on the XY and XZ planes, (b) The view of SNR-B with two Au electrodes (named SNRD-B) on the XZ plane. The white, yellow, green, and blue balls represent H, Si, Au, and P atoms, respectively.

0 eV up to 5 eV with respect to the Fermi level in the SNR-B ($Si_{61}H_{75}P$) with an average diameter of 1.25 nm. The donor ground state is 0 eV in the LUMO state. The excited donor states LUMO+1, LUMO+2, and LUMO+3 are shown in Fig. 2. I denote that the LUMO+i is the ith excited state above the donor ground state LUMO, and the A_1 state is the donor ground state. The T_2 state is the LUMO+2, while the E state is the LUMO+10 state, which is not indicated in Fig. 3.2. Due to the Gaussian broadening in the PDOS spectrum, one PDOS peak may consist of a number of quantum states. The splitting between the A_1-T_2 and T_2-E is 350 meV and 600 meV, which are both much larger than the splitting in the tight binding calculation [62]. Such enhancement of the splitting is common due to the strong quantum confinement of the central-cell donor potential in nano Si [63]. Next, we will study the hybridization of the P electron states and Si electron states in Si nanorods.

Figure 3.3 shows the top and side views of the wavefunctions of the A_1, T_2 and E states in the SNR-B on the XZ and YZ planes, respectively. As we can see, the A_1 orbital has a large projection on the center dopant atom compared to T_2 and E states; therefore, the dopant in the center stabilizes the A_1 state more than the T_2 and E state. This leads to the fact that the donor ground state is the A_1 state. In Fig. 3.3I show the s, p, and d components of the PDOS onto the P atom and onto the first neighboring Si atom in SNR-B. The A_1 state has a contribution not only from the s orbital of the P dopant but also from the p and d orbitals of the first neighboring Si. The T_2 state includes contributions from the p and d orbitals of the P dopant and the s, p, and d orbitals of the first neighboring Si. Finally, the E state has contributions from the s, p, and d orbitals of the P dopant and the s, p, and d orbitals of the first neighboring Si. This means there is hybridization between the P electron states and Si electron states in SNRs. This hybridization can be observed not only at the donor ground state A_1 but also at the donor excited states such as T_2 and E. In bulk Si, the first conductive state is considered as the lowest unoccupied state of the un-doped Si crystals. In nanostructures, there is hybridization between phosphorus electron states and silicon electron states at both donor ground states and donor excited states. The hybridization becomes significantly stronger when the sizes of Si nanostructures are smaller than the Bohr radius of the P donor in bulk Si (around 3 nm) because the electrons are confined by the size of the nanostructures and continue to interact with the P donor in higher-energy excited states. Accordingly, this hybridization must be taken into account to determine the first conductive states in Si nanostructures. The next section will discuss how

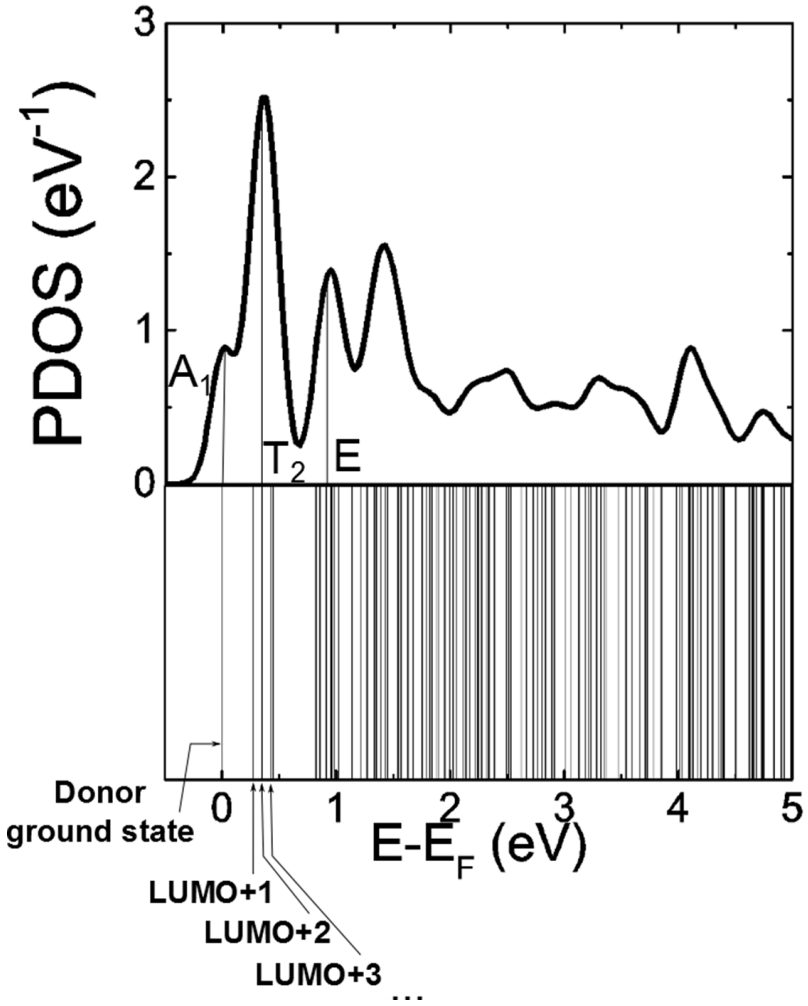

Figure 3.2: Upper: The projected density of states onto the P atom in SNR-B. Lower: the Kohn-Sham energy levels with respect to the Fermi energy, the position of the A_1, T_2, and E states are indicated.

to locate the first conductive states in SNRs and the binding energy of the donor electrons.

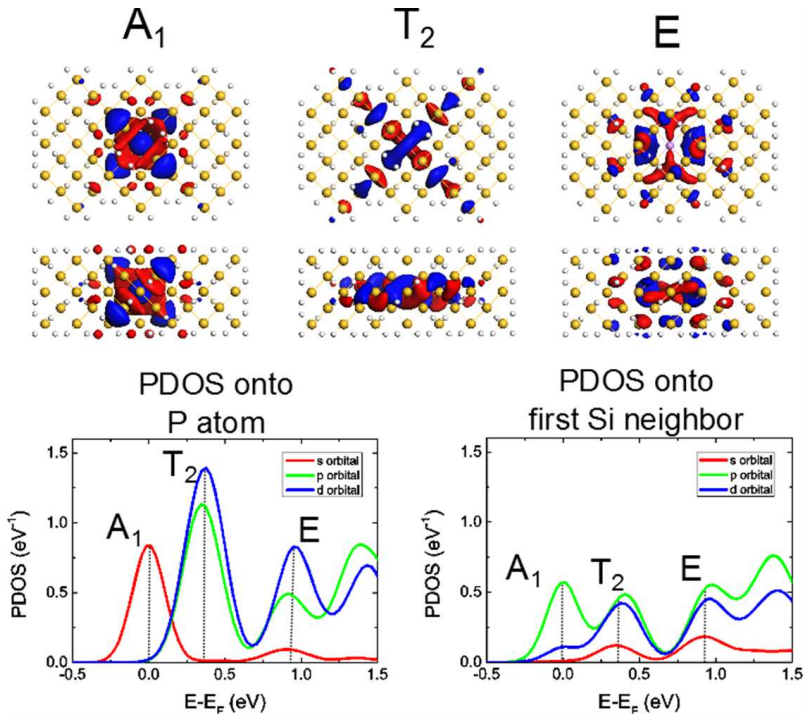

Figure 3.3: Upper: The top and side views of the wavefunctions of the A_1, T_2 and E states in SNR-B on the XZ and YZ planes, respectively; Lower: The s, p, and d components of the PDOS onto the P atom and onto the first neighboring Si atom.

3.4 The first conductive state and binding energy calculation for isolated silicon nanorods

As discussed in the previous section, the phosphorus electron states hybridize with the Si electron states. According to the LCAO theory, the wavefunction of the entire system ϕ is a linear combination of individual atomic orbitals. The weight of the contribution of the phosphorus atomic orbital ϕ_P is important in determining how strongly the donor electrons interact with the P dopant in the nanostructures. Based on the change in the weight of the ϕ_P contribution, we can find the first conductive state relative to the donor ground state. Let us consider which states in the density of states belong to phosphorus atom in a nanostructure. This can be qualitatively considered by using the PDOS, which is obtained by projecting the wavefunction ϕ onto localized atomic orbitals ϕ_P of phosphorus atoms; therefore, the total DOS can be resolved into partial components of PDOS onto individual atoms. The ratio PDOS/DOS, where PDOS is the projected density of states onto the P donor and DOS is the total density of states, presents the relative weight of the states associated with the P dopant compared to the whole system. This ratio can be attributed to the contribution of the P electron states to the states of the whole system. Figure 3.4 shows the PDOS onto the P atoms and the PDOS/DOS ratios for SNR-A, SNR-B, SNR-C, SNR-D, and SNR-E. The five Si nanorods were embedded in large vacuum supercells in order to prevent interactions between the periodic replicas (about 20 Åof vacuum separates neighboring nanorods in the X, Y, and Z directions). The Fermi level was set at 0 eV, and the A_1 donor ground states were set at 0 eV the Fermi level. We can see from Fig. 3.4 that the PDOS/DOS ratios at low energy regimes (below the dashed blue lines) are high and then decrease as energy increases. This can be interpreted as follows: at low energy levels near the donor ground state, the relative weight of the phosphorus electron states is high due to the strong confinement from the atomistic donor potential. At higher energy levels (above the dashed blue line), the relative weight is low due to the decreasing confinement. As a result, the PDOS/DOS ratios decrease almost to zero. Therefore, based on the change in the PDOS/DOS ratios, we can directly estimate the binding energy of the donor electrons in SNRs. I believe that the position of the first conductive state is at the energy level where the PDOS/DOS ratio starts to approach zero. For SNR-A, SNR-B, SNR-C, SNR-D, and SNR-E, the first conductive states are estimated as the positions of the dashed blue lines.

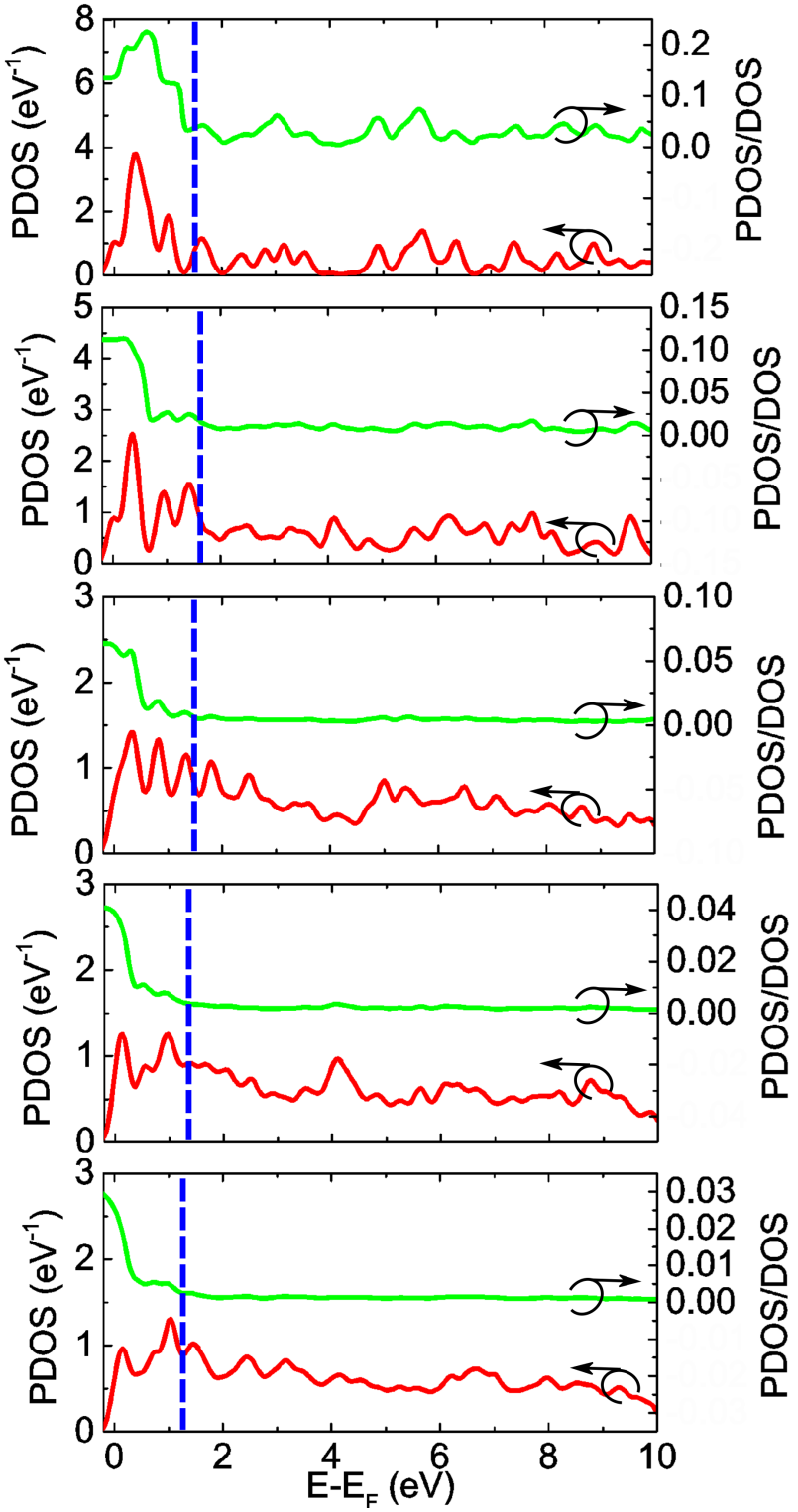

Figure 3.4: The PDOS (red) onto the P atom and the ratio PDOS/DOS (green) of the nanorods SNR-A, SNR-B, SNR-C, SNR-D, and SNR-E. The dashed blue lines present the positions of the first conductive states.

To clarify the exact positions of the first conductive states in SNRs, I have analyzed the 3D wavefunctions associated with the donor ground states and the donor excited states. Figure 3.5 shows the projections of the wavefunction squares along the $< 100 >$ direction associated with the donor ground state and seven donor excited states of nanorod SNR-B: LUMO+3, LUMO+9, LUMO+24, LUMO+28, LUMO+32, LUMO+74, and LUMO+125. For convenient presentation, only seven donor excited states have been shown. Z is the coordinate in the $< 100 >$ direction while the P atom is at the center, which is 15 Å away from the origin. We can see from Fig. 3.5(a) that the projections of the wavefunction squares near the center P atom gradually decrease from donor ground state LUMO to LUMO+28. However from LUMO+28 the decrease cannot be observed clearly. This is consistent with the PDOS analysis that the PDOS/DOS ratio rapidly changes at low energy regimes and then becomes closer to zero at critical energies. The energy level of LUMO+28 is 1.62eV, which is equal to the critical energy (the position of the dashed blue line) found by the PDOS analysis. The right-hand panels in Fig.3.5(a)show the wavefunction visualization of LUMO+28, viewed on the XZ (upper panel) and YZ (lower panel) planes. We can see that the wavefunction of the state LUMO+28 spreads throughout the structure without any significant localization, which suggests that electrons can successfully transport throughout the structures in this state. By combining the PDOS and the 3D-wavefunction analyses, I have found that the energy level of the first conductive state in SNR-B is 1.62 eV. Similarly, the energy levels of the first conductive states in SNR-A, SNR-C, SNR-D, and SNR-E are 1.36 eV, 1.42 eV, 1.36 eV, and 1.21 eV, respectively. The binding energy is calculated as the difference between the A_1 donor ground state and the first conductive state. The A_1 donor ground states were found at the Fermi level 0 eV for the five SNRs, hence binding energies that were equal to the energy levels of the first conductive states in five SNRs. As we can see from Fig. 3.4, the positions of the first conductive states (the positions of the dashed blue lines) do not monotonously increase toward higher energies when the size of the nanorods decrease according to the simple quantum confinement effect. In order to understand the mechanism behind this trend, I have investigated the atomistic effective potential in SNRs. The atomistic effective potential is defined as the sum of the neutral atom potential and the Hartree potential, which considers Coulomb electron-electron interactions [64, 65]. In Fig. 3.5(b) the atomistic effective potential of SNR-B is plotted, and the two arrows indicate the edge of the nanorod. The atomistic effective potential at the P donor site is deeper than that at the Si

sites, which causes the strong localization of the wavefunction of electrons near the P atom site at donor ground state, which is shown with large projections of the wavefunction squares of the LUMO state near the center P atom in Fig. 3.5(a). Figure 3.6 shows the energy levels of the donor ground state and donor excited states along with the atomistic effective potential; we can see that the state LUMO+28 is almost higher than the atomistic effective potential peak at the P atom. Above this peak, the interaction between the donor electrons and the core P ion is small because the electrons are no longer confined by the atomistic effective potential at the P site. As a result, the projections of the wavefunction squares near the P atom remain small from the state LUMO+28 to the higher-energy excited states as we can see from Fig. 3.5(a).

Figure 3.6 shows the atomistic effective potential of SNR-A, SNR-B, SNR-C, SNR-D, and SNR-E. The left panels show the PDOS onto the P atoms, and the positions of the first conductive states with respect to the vacuum level are denoted by the horizontal lines. When the sizes of the nanorods decrease from SNR-E to SNR-A, the first conductive state slightly rises due to the simple quantum confinement effect. However, the interesting thing is that in addition to the simple quantum confinement effect, the atomistic effective potential distribution, which can be reflected into the hybridization of the P electron states and Si electron states, plays a role in determining the energy of the first conductive states. As we can see in Fig. 3.6,the positions of the first conductive states obtained from the PDOS-3DWFs method are still near the peak atomistic effective potential at the P donor site. Except SNR-A with an average radius of 0.35 nm, which is close to the size limit for a P atom while retaining its sp_3 hybridization, the electrons are still confined by the extremely small size of the nanorod and continue to interact strongly with the P atom at high-energy states, even above the top of the atomistic effective potential at the P site. Therefore, the first conductive state for SNR-A is quite far away from the top of the atomistic effective potential. For other larger structures, the electrons can be conductive near the peak atomistic effective potential due to the weaker confinement. When the size decreases from the bulk size to the size of SNR-E (R_{avg} = 1.441 nm), the first conductive state lifts up due to the increase in the quantum confinement and nearly reaches the peak atomistic effective potential at the SNR-E size. Above the peak, the interaction between the donor electrons and the core P ion is reduced. The electron wavefunctions are more delocalized and can attribute to the conduction. If the size continues to decrease however, the first conductive states still stay close to the peaks of the

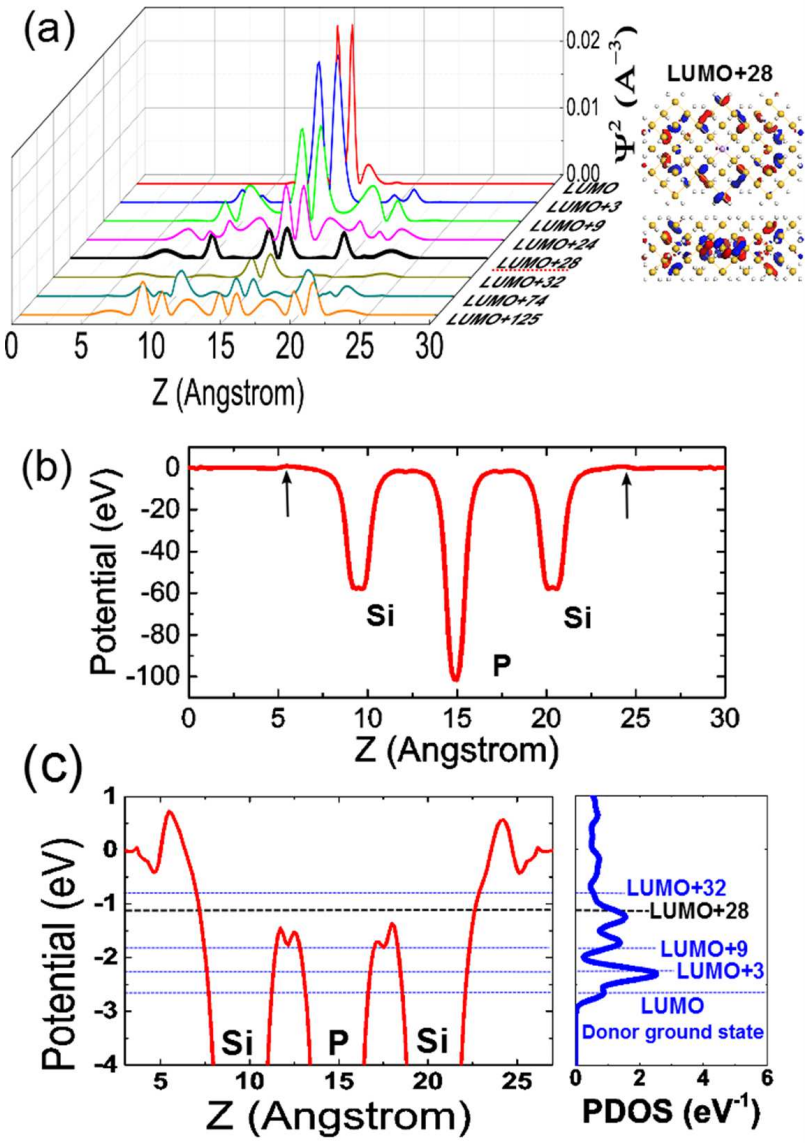

Figure 3.5: (a) The projections of wavefunction squares of the A_1 donor ground state (LUMO) and donor excited states in SNR-B along Z [100] direction, the right panel shows the wavefunction visualization of the donor excited state LUMO+28 viewed on the XZ (upper panel) and YZ (lower panel) planes; (b) The atomistic effective potential of SNR-B along the Z direction, the arrows indicate the edge of the nanorod; (c) The atomistic effective potential of SNR-B along the Z direction plotted with the electronic energy levels, the lines show the positions of the LUMO-donor ground state and the donor excited states.

atomistic effective potentials. As a result, the positions of the first conductive states are weakly dependent on size when the structures are smaller than SNR-E.

According to previous published studies, the binding energies of P donor electrons in Si nanostructures are proportional to the inversed radii of the nanostructures due to the quantum confinement effect. In order to conduct a direct comparison, I calculated the binding energies for the Si nanorods by using the conventional formula: [56]:

$$E^{b}_{conv} = I_d - A_u \tag{3.1}$$

Where $I_d = E_d$(n-1) $-E_d$(n) and $A_u = E_u$(n) $-E_u$(n+1) are the ionization energy and electron affinity of the doped and un-doped systems, respectively. E_d and E_u are the total energy of the doped and un-doped systems.

In this conventional method, the first conductive state is determined as the lowest unoccupied state of the un-doped Si nanostructure. Hence, it fails to include the hybridization of the phosphorus electron states and Si electron states at the first conductive states; the binding energy obtained by this method is simply a decreasing function of the size due to the simple quantum confinement effect. Figure 3.7 shows the binding energy of the dopant electrons as a function of the nanorods average radius, which is calculated by using both the PDOS-3DWFs method and the conventional method. From Fig. 3.7 we can see that the conventional method shows a non-linear decrease in the binding energy when the size increases, whereas the PDOS-3DWFs method results in a binding energy of approximately 1.5 eV, which is virtually unaffected by the nanorods dimensions. In extremely small nanostructures that are smaller than about 1.4 nm, the energy levels of the first conductive states are capped near the peak atomistic effective potential at the P donor site, even for the smallest nanorod SNR-A. As a result, the binding energy calculated by the PDOS-3DWFs method shows virtual independence from the size, as can be seen from Fig. 3.7. This fact signifies good tolerance of the binding energy, which governs the operating temperature of single dopant-based transistors.

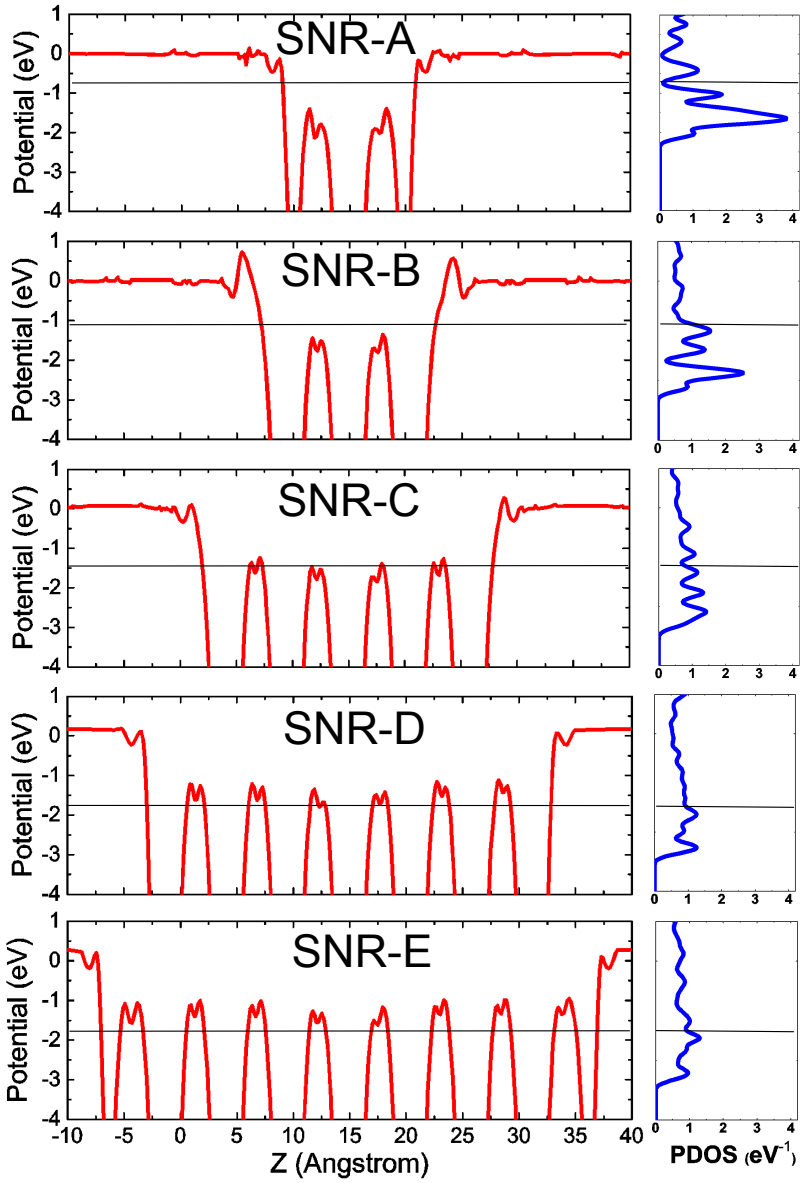

Figure 3.6: The atomistic effective potential of the SNR-A, SNR-B, SNR-C, SNR-D, and SNR-E. The right side shows the PDOS onto the P atoms. The energy of the first conductive states with respect to the vacuum level is presented by the horizontal lines.

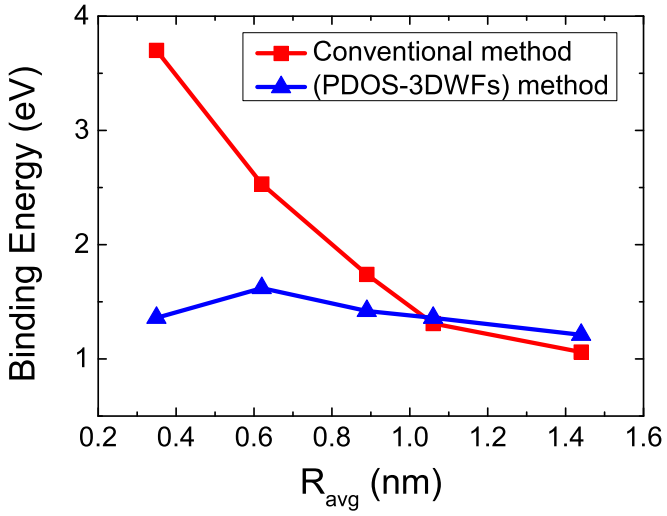

Figure 3.7: The binding energy of the donor electrons as a function of the nanorods average radius calculated by using the PDOS-3DWFs method and the conventional method. The lines are only for eye guide.

3.5 The first conductive state and binding energy calculation for silicon nanorods sandwiched with two gold electrodes

In this section, I study single P-doped Si nanorods sandwiched with two semi-infinite Au electrodes as indicated in Fig. 1(b) in order to discuss the donor electron binding energy in terms of the transmission spectra. The Si nanorods are labeled with the electrodes $Au - Si_{12}H_{28}P$, $Si_{61}H_{75}P - Au$, $Au - Si_{167}H_{147}P - Au$, $Au - Si_{357}H_{243}P - Au$, and $Au - Si_{652}H_{364}P - Au$ as SNRD-A, SNRD-B, SNRD-C, SNRD-D, and SNRD-E, respectively. Figure 3.8 shows the PDOS onto the P atoms of SNRD-A to SNRD-E. The energy of the donor ground states is marked by the dashed purple lines. In these calculations without any bias between the left and the right leads, the Fermi levels of the left and the right leads were set at 0 eV and the donor ground states were then shifted to above the Fermi energy levels. Compared with the PDOS spectra for SNRs in Fig. 3.4, the individual peaks in the PDOS spectra obtained for SNRDs are broader. This is presumably caused by the broadening of quantum energy levels of SNRs induced by the electrodes, which is the estimated part of the self-energies of the electrodes. Moreover, the amplitudes of the PDOS at low energy regimes near the donor ground states gradually decrease from SNRD-

A to SNRD-E, reflecting the gradual delocalization of the wavefunction of the donor electrons. Therefore, the evolutions of the PDOS with respect to energy can be used to estimate the binding energy of electrons, as discussed in the previous section.

To prove the validity of the PDOS-3DWFs method in the previous section, I have undertaken transport calculations for electrons through the Si nanorods with two electrodes. The transmission rate T(E) is calculated according to the Landauer formula, which is implemented using the OpenMX code. Figure 3.9 shows the transmission spectra (blue) and the corresponding atomistic effective potentials (red) for the five SNRDs; in these plots, the vacuum level was set as 0 eV. The positions of the P, Si, and Au atoms along the Z direction are also indicated, and the energy of the donor ground state D0 is indicated by the lower horizontal black lines. We can see from Fig. 3.9 that the transmission rates are very low at the energy of the donor ground states and increase dramatically as the energy increases. This is due to the strong contributions of P electron states near the donor ground states, which causes the strong concentrations of electrons at the P donor sites. The low transmission peaks near the donor ground states D^0 reflect the transportation of single-electron tunneling mediated by single dopants [13]. The transmission rates increase as energy increases because the contributions from the P electron states gradually decrease, leading to greater wavefunction delocalization in the donor electrons. To find the positions of the first conductive states, we define the positions where the transmission rates exceed one (100

In Fig. 3.10,the binding energies of the five devices from SNRD-A to SNRD-E calculated from the transmission spectra are compared with those of the five isolated Si nanorods from SNR-A to SNR-E, calculated using the PDOS-3DWFs method. The green squares represent the binding energies for SNRDs, while the blue triangles indicate the binding energy for SNRs. The virtual R_{avg} independence binding energy can be seen clearly for both methods. The binding energies are found at around 1.5 eV. This can be attributed to the capping of the first conductive states near the tops of the atomistic effective potentials at the P donor site. In my transport calculation, the transmission via state H_0 describes the transportation of electrons via the donor ground state H_0. The transmission via H_1 on the other hand describes the transportation of electrons via state H_1. The different energy between H_0 and H_1 is the excitation energy for electrons from H_0 to H_1. In this calculation, I define the first conductive state (CS) as when the transmission rate begins to equal 100As for the operation of single dopant devices, the isolated current peak at a

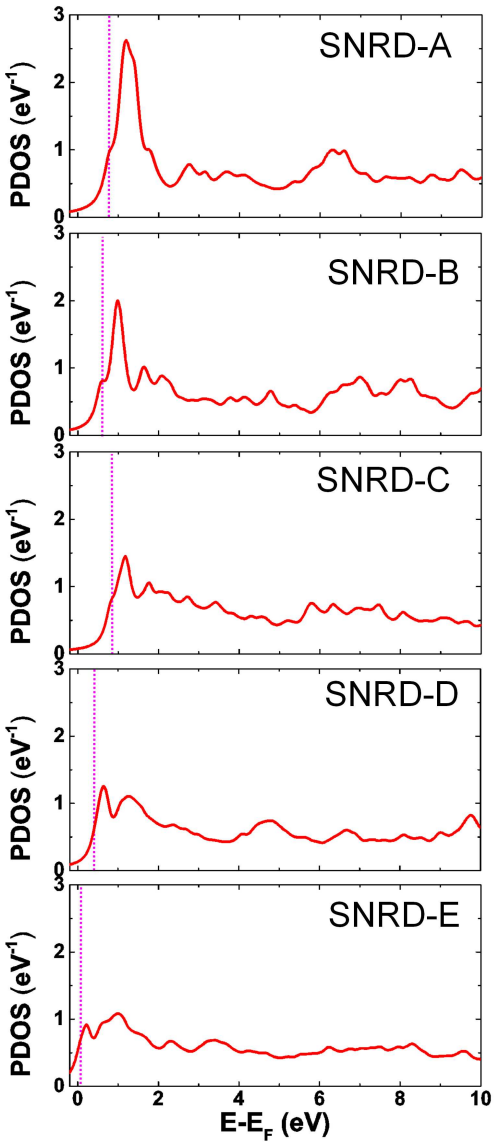

Figure 3.8: The PDOS onto the P atom of five Si nanorods sandwiched with two electrodes SNRD-A to SNRD-E. The dashed purple lines present the positions of the donor ground states..

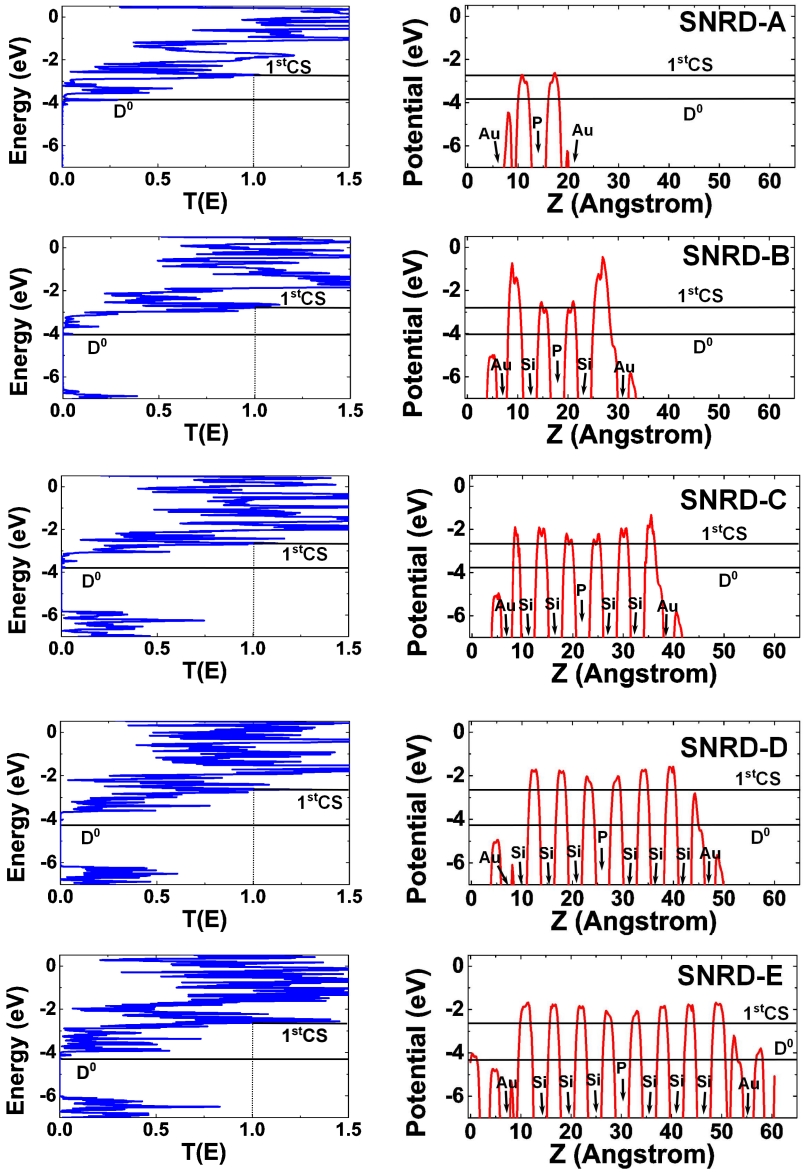

Figure 3.9: left panels: the transmission rates T(E); right panels: the corresponding atomistic effective potentials of the SNRD-A to SNRD-E. Two black lines show the positions of the donor ground states D^0 (the lower lines) and the first conductive states 1st CS (the upper lines). .

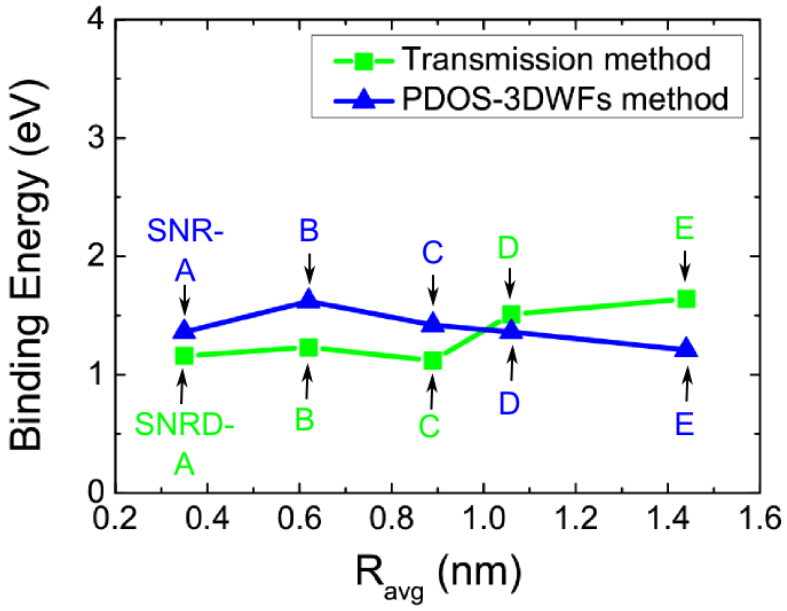

Figure 3.10: The binding energies of the donor electrons as a function of the nanorods average radius. The green squares and blue triangles represent the binding energies for SNRDs and SNRs calculated by the transmission method and the PDOS-3DWFs method, respectively. The lines are only for eye guide..

certain temperature can be considered as the tunneling current via an individual dopant; therefore, the barrier energy required for electrons to tunnel via a single dopant is particularly important. The new definition of the first conductive state has been introduced in order to calculate this kind of barrier energy.

3.6 Conclusion

I have studied the electronic properties of single P-doped Si nanorods by using the DFT calculation. It has been determined that the hybridization of the donor electron states and the Si electron states is significant, not only at the donor ground state but also at donor excited states in Si nanorods. The PDOS-3DWFs analysis has clarified the gradually decreasing contribution of the phosphorus electron states from the donor ground states to the higher-energy donor excited states. I have defined the first conductive state as the point at which electrons start to fully pass through the structure. As for the operation of single dopant devices, the isolated current peak at a certain temperature can be considered as the tunneling current via an individual dopant. Therefore, the barrier energy required for electrons to tunnel via a single dopant is especially important. A new definition of the first conductive

state has been introduced in order to calculate this kind of barrier energy. By using the PDOS-3DWFs analysis, I have been able to identify the first conductive states. The binding energies of the donor electrons in the single P-doped Si nanorods, which have an average radius of smaller than 1.4 nm, have been calculated as the difference between the first conductive state and the donor ground state. It has been found that the binding energy is around 1.5 eV while the conventional method results in an increasing function by reducing the nanorod's radius. The difference is due to the fact that the conventional method does not include the hybridization between the donor electron states and Si electron states at the first conductive state. As the radius decreases below 1.4 nm, the first conductive state is capped near the top of the atomistic effective potential at the P donor site. Above the potential peak, the interaction between the donor electrons and the core P ion is significantly reduced, while the interaction between donor electron states and Si electron states increases. Therefore, the electron wavefunctions above the top are more delocalized and can attribute to the conduction. This causes the binding energy in small nanorods that are smaller than 1.4 nm to be weakly dependent on the size when the size continues to decrease. This fact signifies the good tolerance of the binding energy, which governs the operating temperature of single dopant-based transistors in practice. The transmission spectra, which reflects the transport properties of electrons in Si nanorod devices, shows consistent results with the PDOS-3DWFs method and this fact proves the validity of the new method. This study has been published in the Journal of Applied Physics **116** (6), 063075 (2014).

Chapter 4

Single phosphorus-doped cross-shaped silicon nanotructures

4.1 Introduction

In this chapter, I discuss how to estimate the binding energy of phosphorus electrons in single phosphorus-doped cross-shaped silicon nanostructures by using the PDOS-3DWFs method mentioned in Chapter 3. Recent progress in silicon nanotechnology has allowed electrical measurements of electron or hole tunneling through individual dopants in the channel of silicon transistors [23, 67, 37, 68, 69, 12, 70], and one of the basic operations of these nanometer-scale devices is based on single-electron tunneling mediated by a single dopant. The binding energy of donor electrons should be much higher than the thermal energy to ensure the operation of single dopant devices at room temperature. However, there are no reports on tunneling operation via dopants at elevated temperatures, even though a higher tunneling operation temperature is crucial for applications using CMOS-based electronics. The results reported so far have been mostly obtained for transistors that have channels without any special patterns [23, 67, 37, 68, 69, 12, 70]. Aiming at high temperature operation of electron tunneling via a single donor, the Tabe group from Shizuoka University designed single-donor transistors with nano stub-shaped channels in which the tunnel barrier height is enhanced due to dielectric confinement. In this project, I contribute the first-principles calculation discussed in this chapter; the PDOS-3DWFs method is applied to estimate the binding energy of phosphorus electrons in single phosphorus-doped cross-shaped silicon nanostructures, which are similar to real nano stub-shaped channels in shape but

much smaller.

4.2 Structures of the cross shaped silicon nanotructures

The single phosphorus-doped cross-shaped silicon nanostructures used in this study are built with the < 100 > orientation in the X direction. The structures are covered by H atoms in order to passivate all of the dangling bonds. To investigate the effect of the position of the P atom on the electronic and transport properties, we built Si structures $Si_{96}PH_{130}$ - with different P atom positions. In all of these structures, we have studied the P atom at the central substitutional site, the off-central substitutional site, and the substitutional site at the edge. These three models are labeled as SNC-z+0, SNC-z+2, SNC-z+4. Figure 4.1(a)shows the views of SNC-z+0 on the XY and XZ planes. The SNCs have been embedded in large supercells in order to prevent interactions between the periodic replicas (about 20 Å of vacuum separates neighboring clusters in the X, Y, and Z directions). To build Si nanostubs with two electrodes, we used two semi-infinite Au nanowires as the left and right leads as shown in Fig. 4.1(b). The channels are SNCs. Due to the large scale calculation, the number of Au atoms in each lead is optimized to be 24. The distance between the lead interfaces and the nanorods is about 2.0 Å. The X < 100 >direction has been set as the transport direction from the left lead to the right lead. To minimize the hybridization between the states from two electrodes and the states of the nanorods, fully hydrogen terminated Si nano were used. Fig. 4.1(c) shows the positions of the P atom when it moves from the center to the edge.

4.3 The projected density of states - 3D wavefunctions analysis

Figure 4.2 shows the PDOS onto the P atoms and the PDOS/DOS ratios of SNC-z+0, SNC-z+2, and SNC-z+4. The three cross-shaped Si nanotructures were embedded in large vacuum supercells in order to prevent interactions between the periodic replicas (about 20 Å of vacuum separates neighboring nanorods in the X, Y, and Z directions). The Fermi level is set at 0 eV, and the A1 donor ground states are at this level. We can see from Fig. 4.2 that the PDOS/DOS ratios at low energy regimes

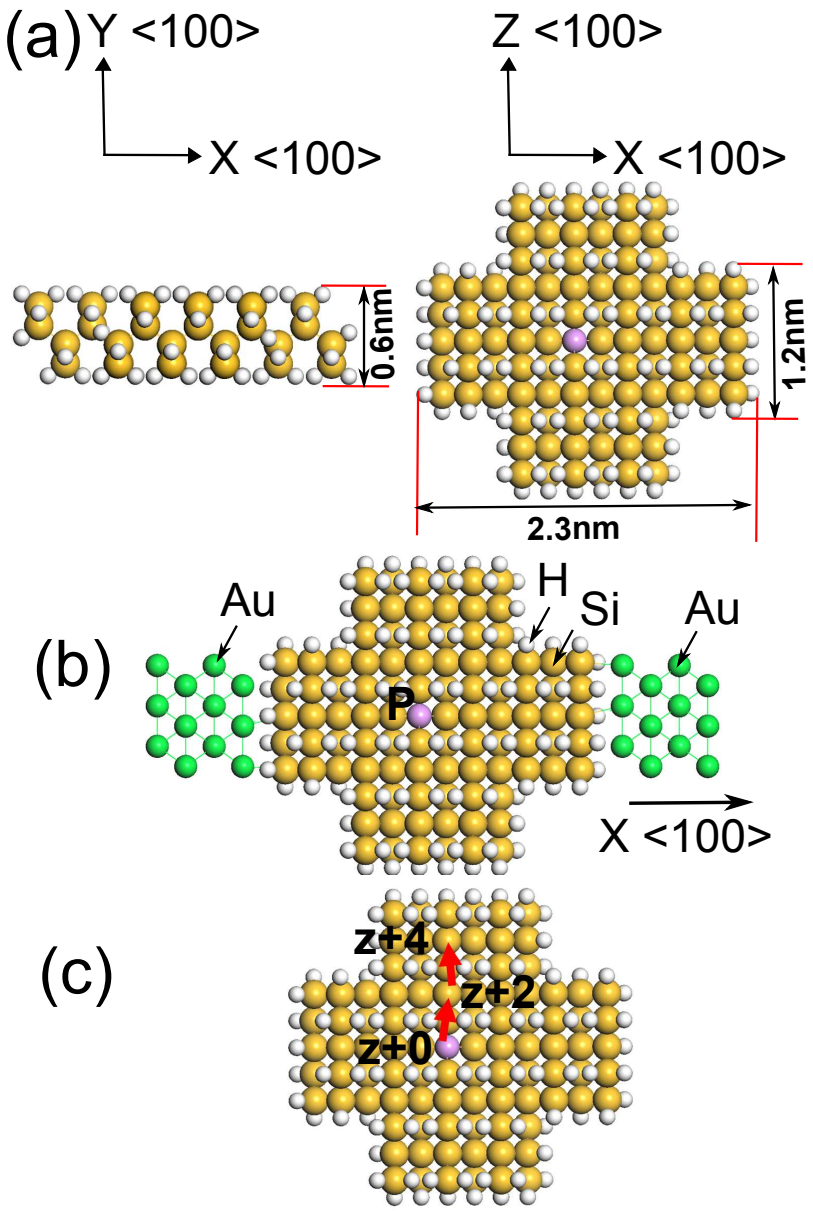

Figure 4.1: (a) The single P-doped cross-shaped Si nanostructure SNC-z+0 ($Si_{96}PH_{130}$) viewed on the XY and XZ planes, (b) The view of SNC-z+0 ($Si_{96}PH_{130}$) with two Au electrodes on the XZ plane, (c) The positions of the P atom when it moves from the center substitutionl site to the edge substitutionl site. The white, yellow, green, and blue balls represent H, Si, Au, and P atoms, respectively.

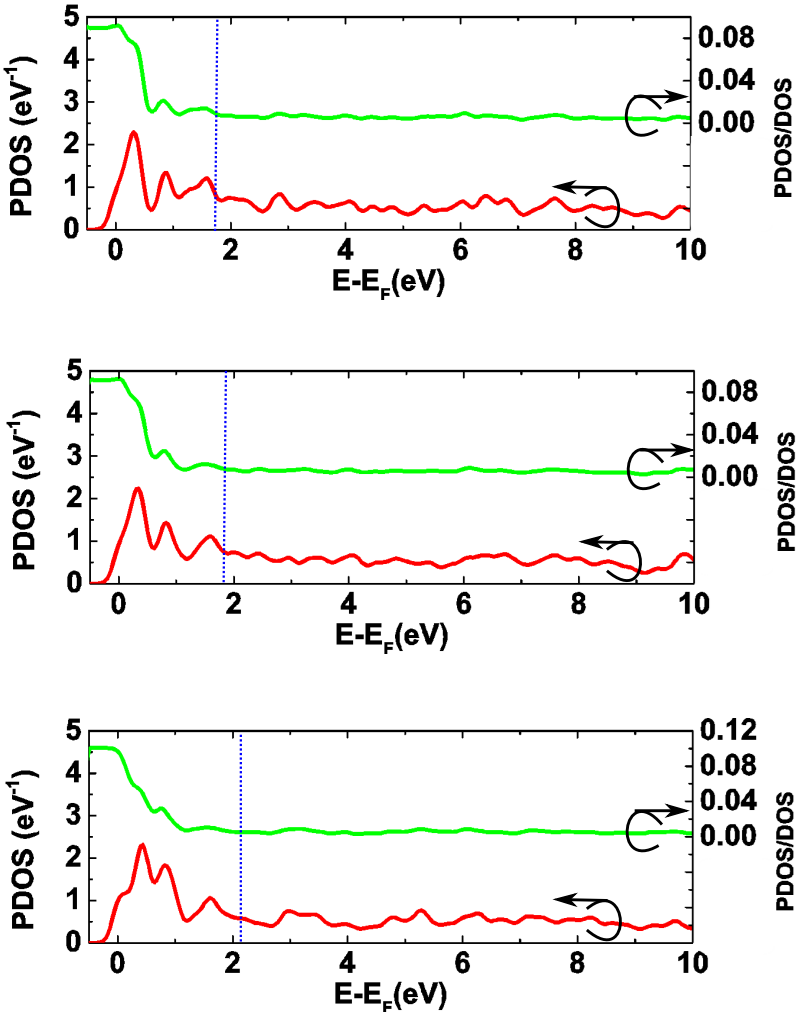

Figure 4.2: The PDOS (red) onto the P atom and the ratio PDOS/DOS (green) of the SNC-z+0, SNC-z+2, and SNC-z+4. The dashed blue lines present the positions of the first conductive states.

(below the dashed blue lines) are high and then decrease as energy increases. This is due to the fact that at low energy levels near the donor ground state, the relative weight of the P electron states is high due to the strong confinement from the atomistic donor potential. At higher energy levels (above the dashed blue lines), the relative weight is low due to the decreasing confinement. As a result, the PDOS/DOS ratios decrease nearly to zero.

To clarify the exact positions of the first conductive states in SNCs, I have analyzed the 3D wavefunctions associated with the donor ground states and the donor excited states. Figure 4.3 shows the wavefunction visualization along the Y direction for the donor ground state at 0 eV and for donor excited states at higher energies. The blue and red represent the positive and negative parts of the

wavefunction. All wavefunctions were visualized with the fixed isovalue of 0.015. For convenient presentation, we only show some selected donor excited states. We can see from Fig. 4.3 that the wavefunction at the donor ground state is strongly localized around the P atom. For the structure SNC-z+0, the wavefunction is gradually delocalized at energy levels higher than 0.81 eV. It is evident that above 1.81 eV the wavefunction becomes fully distributed within the entire volume of the structure. For the structure SNC-z+2, the wavefunction gradually spreads around when energy increases from 0 eV to 0.79 eV and continues to spread. From 1.92 eV, the wavefunction can be considered as fully distributed. Finally, for the structure SNC-z+4, which has a P atom at the wing of the channel, the wavefunction gradually spreads around when energy increases from 0 eV to 1.82 eV. Even at higher energy levels than 1.82eV, the wavefunction still does not spread entirely within the structure. From 2.20 eV the wavefunction becomes fully distributed, which can be explained as follows: when the P atom is located at the wing of the channel, it is more difficult for the wavefunction to spread entirely within the structure, especially in the horizontal direction. As a result, higher energy is needed for the first fully distributed wavefunction.

From the PDOS and the 3D-wavefunction analyses, I have found that the energy levels of the first conductive state in SNC-z+0, SNC-z+2, and SNC-z+4 are 1.81, 1.92 and 2.20eV, respectively. The binding energy is calculated as a difference between the A_1 donor ground state and the first conductive state. The A_1 donor ground states were found at the Fermi level 0 eV, hence the binding energies are equal to the energy level of the first conductive states. According to previous published studies [56, 66], the binding energies of P donor electrons in Si nanostructures are proportional to the inversed radii of the nanostructures due to the quantum confinement effect. In order for a direct comparison, we have calculated the binding energies for the Si nanorods by using the conventional formula [56]:

$$E^b_{conv} = I_d - A_u \tag{4.1}$$

Where $I_d = E_d$(n-1) $-E_d$(n) and $A_u = E_u$(n) $-E_u$(n+1) are the ionization energy and electron affinity of the doped and un-doped systems, respectively. E_d and E_u are the total energy of the doped and un-doped systems.

Figure 4.4 shows the binding energy of the dopant electrons as a function of the position of the P atom, which is calculated by using both the PDOS-3DWFs method and the conventional method. From Fig. 4.4 it is evident that the conven-

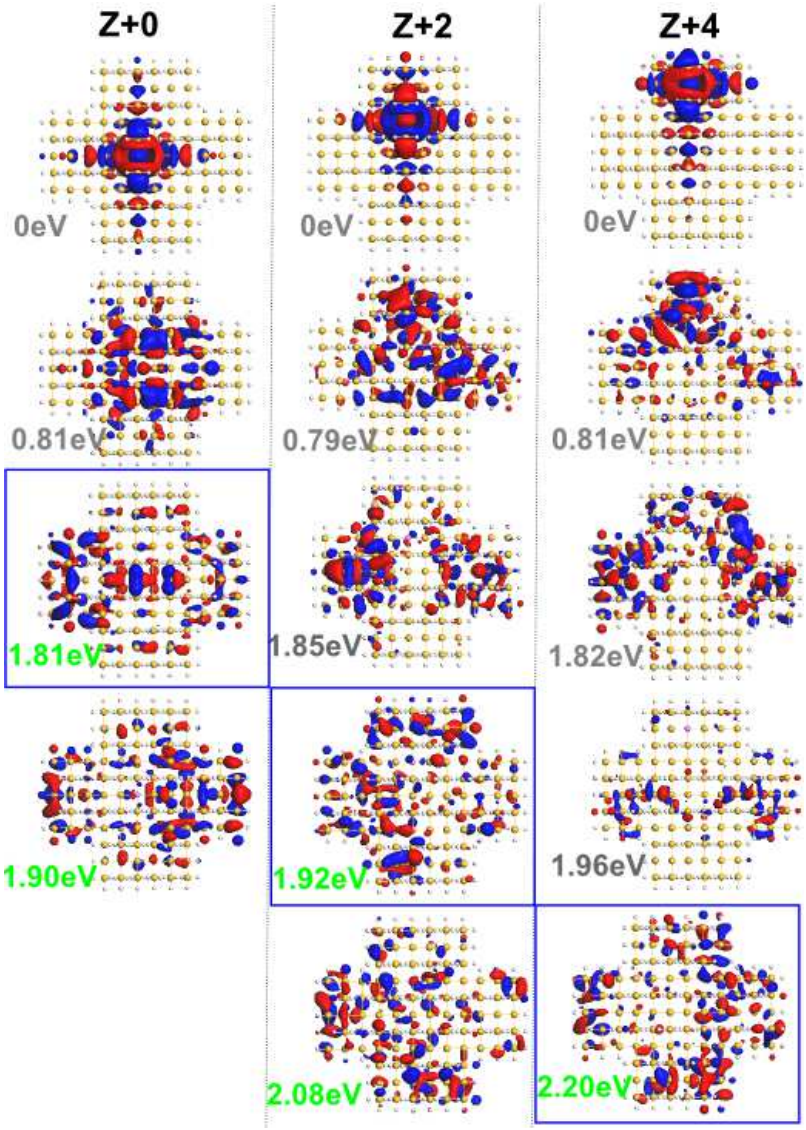

Figure 4.3: The wavefunction visualization along the Y direction associated to the donor ground state at 0eV and donor excited states at higher energy. The blue and red represent the real and imaginary part of the wavefunction. All wavefunctions were visualized with the isovalue of 0.015.

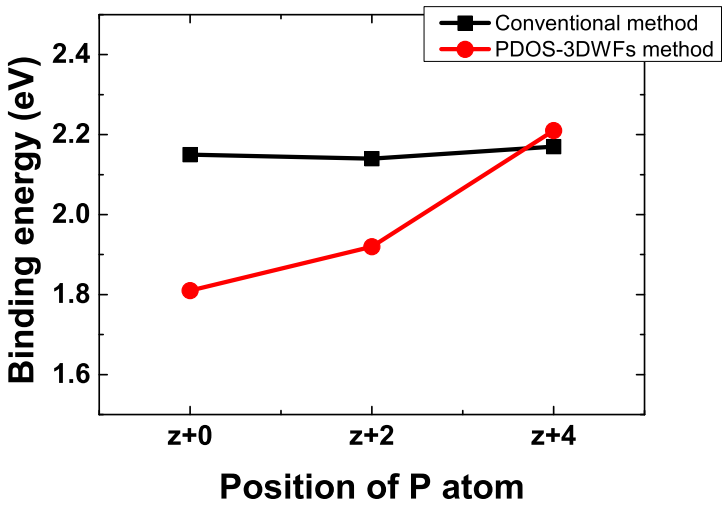

Figure 4.4: The binding energy of the dopant electrons as a function of the position of the P atom, which is calculated by using the PDOS-3DWFs method (red) and the conventional method (black). The lines are only for eye-guide.

tional method shows a binding energy of approximately 2.1 eV, which is virtually independent from the position of the P atom. The PDOS-3DWFs method results in an increased binding energy when the P atom moves toward to the edge. In the conventional method, the first conductive state is determined as the lowest unoccupied state of the un-doped Si nanostructure. Hence, it fails to include the impact of the P position on the energy of the first conductive states. The binding energy obtained by this method is unchanged when the P atom moves from the center to the edge.

4.4 Experimental study of Si nano-stubshape transistor

In this section, I will discuss the experimental study of Si nano-stub shape transistors. These studies were done by Shizuoka University's Tabe group, and the results were published in [13, 14]. In this project, I have contributed to the first-principles calculation as discussed above.

The structure of silicon-on-insulator field-effect transistors (SOI-FETs) is shown in Fig 4.5. The top Si layer is n-type doped by thermal diffusion with phosphorus to a concentration of N_D =1x10^{-18} cm^{-3}. The TEM image shows the ultra-thin

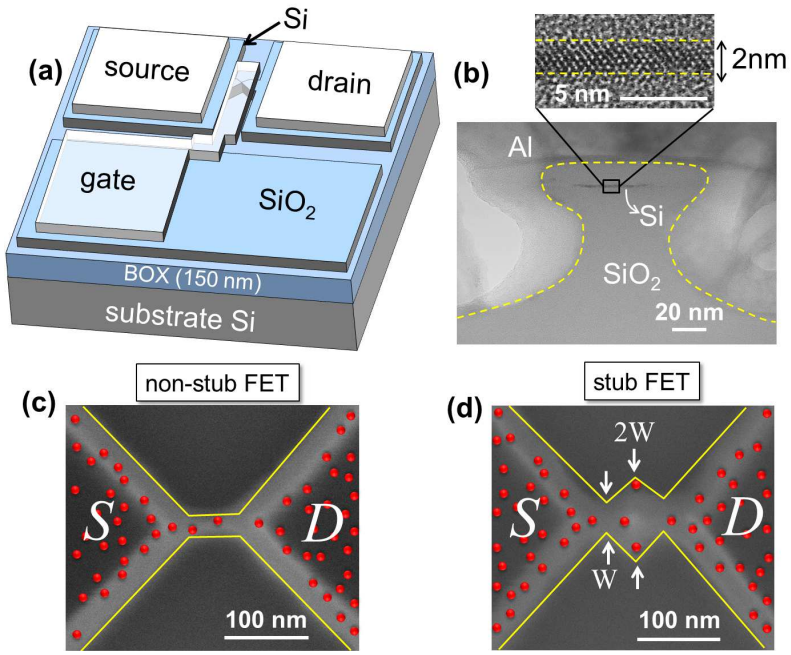

Figure 4.5: (a) Birds eye view of silicon-on-insulator transistor under study. (b), Cross-sectional TEM image taken across the device channel (higher-resolution image of the channel is shown in the float-up, indicating the thickness of the top Si layer of about 2 nm). (c), (d), Scanning Electron Microscope (SEM) images before final oxidation for smallest devices with: non-stub channel (c) and stub channel (d). The solid lines mark the edges of the channels. P donor atoms within the channel and adjacent source (S) and drain (D) pads are schematically shown as dots.After [13].

SOI channel (around 2 nm). The width W for the stub-channel is the width of the narrow constrictions, while the width across the stub region is designed to be 2W. Figure 4.6 shows the temperature dependence of $I_D - V_G$ characteristics with both a non-stub channel (15-300 K) and a stub-channel (16-220 K). At the lowest temperatures (around 15 K), the $I_D - V_G$ characteristics exhibit a number of isolated current peaks, which are the result of electron tunneling transport via donor induced quantum dots forming in the channel. In Figs. 4.6(c) and 4.6(d), for clarity, only the temperatureassociated lowest-V_G current peaks are extracted from the full $I_D - V_G$ characteristics and are plotted in the V_G-temperature plane. These peaks appear successively with increasing temperatures and are ascribed to tunneling via P donors with deeper ground-state energies. With increasing temperature however, due to the broadening of the Fermi-Dirac electron distribution in the reservoir as illustrated in Fig.4.6(e), the tunneling rate is enhanced and the corresponding current peaks successively emerge, exceeding the detectable current level. It has been determined that, for the stub-channel FET, the last emerging current peak appears at T=100 K [Fig. 4.6(d)].

Tunnel barrier heights ($E_{barrier}$) were extracted from the Arrhenius plots of I_D for elevated temperatures ($T > 150K$). For a V_G value corresponding to a current peak, $E_{barrier}$ represents the energy difference between the donors ground state and the potential barrier maximum along the source-drain direction, as illustrated in Fig.4.6(e)(left panel). In Figs.4.6(c) and4.6(d), these extracted $E_{barrier}$ values are shown on top of each emerging current peak. The barrier energy was calculated according to the Arrhenius equation:

$$\ln I_D = \ln AT^2 - \frac{E_{barrier}}{k_B T} \tag{4.2}$$

where A is a parameter.

It is worth mentioning that the stub-channel FET with the narrowest W has the highest barrier energy. This energy systematically decreases for the stub-channel FETs with larger W as highlighted in Fig 4.7. This fact suggests that a higher barrier energy is ensured when donors can be located in the sharp corners of the narrowest sub-channel. This is because in such locations P donors experience both the dielectric confinement effect and the quantum confinement effect. The P dopants are more confined at the edge of the narrowest stub-channel transistor in comparison to wider stub-channel transistors. These results are consistent with the DFT calculation of the binding energy for the single P-doped cross-shaped Si

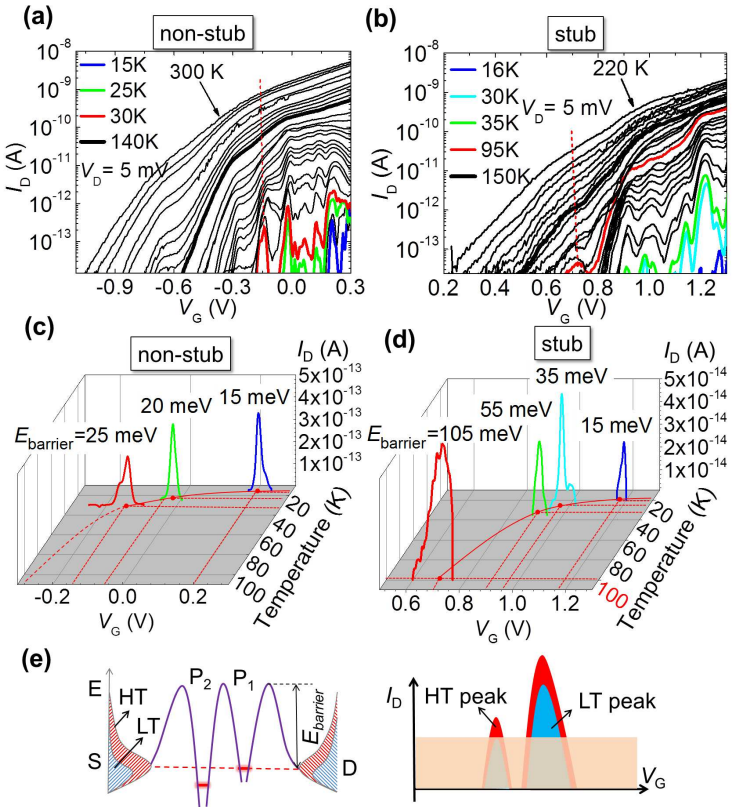

Figure 4.6: (a), (b), Temperature dependence of $I_D - V_G$ characteristics (V_D = 5 mV) for smallest devices with: (a), non-stub channel (20-300 K) and (b), stub channel (20-220 K). At lowest temperature, isolated current peaks can be observed. As temperature is increased, new current peaks at negatively larger $_{VG}$s become measurable. (c), (d), Emerging current peaks extracted as a function of temperature for transistors with: non-stub channel (c) and stub channel (d). Each current peak corresponds to tunneling via a different P donor, with activation energy as indicated in the graph. Most remarkably, for the stub-channel transistor in (d), last-observable current peak (at V_G = 0.7 V) emerges at T = 100 K. (e), Schematic illustration of single-electron tunneling via a P donor atom (P2). Transport via the deepest-energy P donor (P1) cannot be detected at low temperatures (LT), at which the peak is buried below the noise level, but the current peak emerges at higher temperatures (HT). After [13].

nanostructures; when the P atom is located at the edge of the nanostructures, it is likely more difficult for the wavefunction to spread entirely within the structure, especially along the horizontal direction as discussed in the DFT calculation. The positional dependence of the P donor therefore results in higher barrier energy in stub-channel transistors.

Although the dielectric confinement effect is not considered in the PDOS-3DWFs method, the similar trends in the results of the ab-initio calculations in the previous section and the experimental results is clear. In the ab-initio calculations, the binding energy for the case P atom at the edge is higher than that for the case P atom at the center of single P-doped cross-shaped Si nanostructures. This can be interpreted as a result of the positional dependence of the binding energy on the dopant. When the P atom is situated at the edge of the nanostructure, it becomes more difficult for the wavefunction to spread entirely within the structure, especially along the horizontal direction. Therefore, higher energy is needed for the first fully distributed wavefunction. For the stub-channel FETs, the barrier energy attracted from the ID-VG characteristics shows a higher value for the conventional straight channel transistor, which is due to the fact that P donors experience at the stub locations.

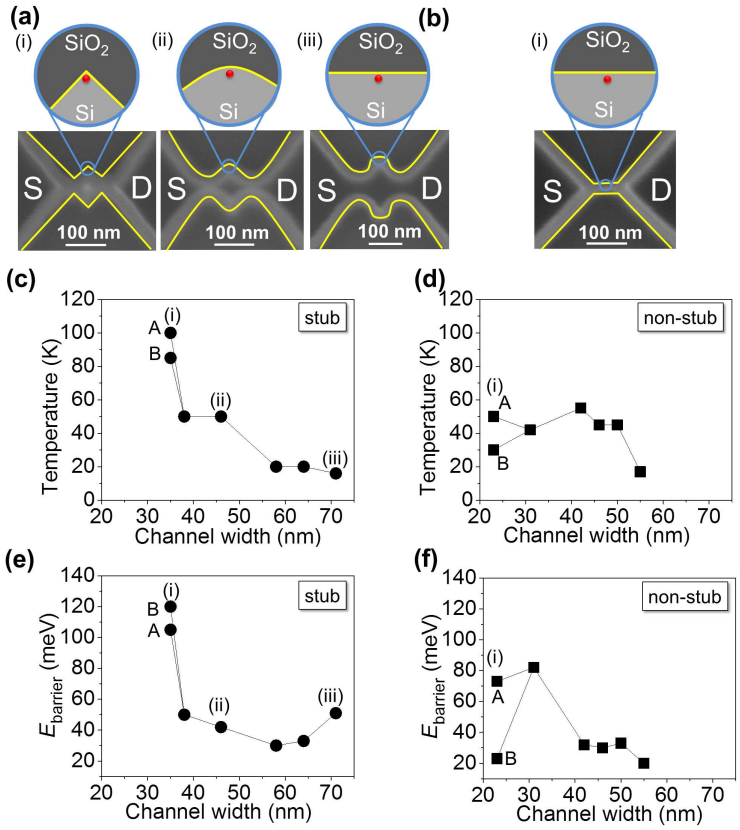

Figure 4.7: (a), (b), Temperature of emergence of the final peak for devices with: stub channel (a) and non-stub channel (b). Data is plotted as a function of channel width, in which each data point corresponds to a different device (A and B indicate two different devices with nominally same dimensions). SEM images and their zoomed-in sketches show that the shape of the stub area changes from round to pointed-hat as the channel width decreases, and the ratio of SiO_2 to Si increases, as indicated by (iii), (ii), and (i) in (a). For pointed-hat shape device, a P donor is mostly surrounded by SiO_2. Therefore, tunnel barrier is enhanced due to strong dielectric confinement effect. As a result, high-temperature current peak (100 K) appears (a). For non-stub device, the SiO_2 to Si ratio is almost constant with respect to channel width. Dielectric confinement effect is less dominant and, as a result, all the high-temperature peaks are below 60 K (b). (c), (d), Activation energy extracted for the lowest-energy P donor (for V_G corresponding to the last-observable emerging peak) as a function of channel width for devices with stub channel (c) and non-stub channel (d). After [13].

4.5 Conclusion

The binding energy of phosphorus electrons in the single P-doped cross-shaped Si nanostructures have been calculated using the DFT framework. I have defined the first conductive state as where electrons start to fully transport through the structure. As for the operation of single dopant devices, the isolated current peak at a certain temperature can be considered as the tunneling current via an individual dopant. Therefore, the barrier energy required for electron can tunnel via single dopant is particularly important. This new definition of the first conductive state is introduced in order to calculate this kind of barrier energy. By using the PDOS-3DWFs analysis, I have been able to identify the first conductive states. The binding energies of the donor electrons in the single P-doped cross-shaped Si nanostructures have been calculated as the difference between the first conductive state and the donor ground state at 0 eV. I have found that the binding energy increases when the P atom moves from the center toward to the wing, while the conventional method suggests an independent function by changing the P position. The difference is due to the fact that the conventional method does not include the impact of the P position on the energy of the first conductive state. When the P atom is situated at the wing of the channel, it is more difficult for the wavefunction to spread entirely within the structure, especially in the horizontal transport direction. As a result, higher energy is needed for the first fully distributed wavefunction. The barrier energy (binding energy) for the experimental stub-channel FET is higher than that for the conventional straight channel FET, which is consistent with the computational study of the single P-doped cross-shaped Si nanostructures. In the ab-initio calculations, the binding energy for the case P atom at the edge is higher than that for the case P atom at the center. This can be interpreted as a result of the positional dependence of the binding energy on the dopant. When the P atom is located at the edge of the channel, it becomes more difficult for the wavefunction to spread entirely within the structure, especially along the horizontal direction. Again, this means that higher energy is needed for the first fully distributed wavefunction. For the stub-channel FETs, the barrier energy attracted from the I_D-V_G characteristics shows a higher value for the conventional straight channel transistor. This comes from the fact that P donors experience at the stub locations.

Chapter 5

Phosphorus-boron co-doped silicon nanostructures

5.1 Introduction

Recently, the co-doping of Si nanocrystals with P and B has been studied intensively with the aim of tuning the optical properties of Si nanocrysals [71, 72, 73, 74, 75, 76, 77, 78, 79]. Experimental studies show that it is possible to control the Si-nc photoluminescence by simultaneous doping with n- and p-type impurities [77, 78, 79]. Theoretical studies [71, 72, 73] demonstrate that co-doping significantly reduces the nanocrystal bandgap and presents the valence and conduction band edge states, which can establish optical transition and qualitatively consistent with the experimental studies. Another aim of studying P-B co-doping in Si nanocrystals is to utilize the electronic and transport properties of nanoscale p-n junctions [74, 80, 42]. Through further reduction in the size of nanoscale p-n junctions, the impact of P and B as individual dopants on the electronic and transport properties will undoubtedly become more significant. Although a theoretical study on the electronic and transport properties of nanoscale pn junctions in term of the impact of individual dopants on these properties is required, such a study has not yet been reported. In this chapter, I perform first-principles calculations to investigate the electronic and transport properties of phosphorus and boron co-doped silicon nanostructures.

5.2 Structures of the phosphorus-boron co-doped silicon nanostructures

Fig. 5.1(a) shows the top and side view of the isolated P-B co-doped Si nanorod. The Si nanorod (SNR) was built with the < 100 > orientation along the X direction, and the H atoms were used to passivate all of the dangling bonds on the surface. I place the phosphorus and boron atoms at substitutional sites. The SNR was embedded in large supercells in order to prevent interactions between the periodic replicas (about 20 Å of vacuum separates neighboring clusters in the X, Y, and Z directions). The structures have 601 atoms in total. The number of silicon atoms and dopants is 357. To build a two-terminal SNR, I used two semi-infinite Au nanowires as the left and right lead as shown in Fig. 5.1(b). Fig. 5.1(c) shows the positions of the P and B atoms when the distances between them change. Due to the large scale calculation, the number of Au atoms in each lead is optimized at 20. The distance between the lead interfaces and the SNR is about 1.5 Å, while the X < 100 > direction is set as the transport direction from the left to the right lead. To minimize the hybridization between the electronic states of two electrodes and the electronic states of the SNR, fully hydrogen terminated SNR was used.

5.3 The atomistic buit-in potential in phosphorus-boron co-doped silicon nanorods

First, let us discuss the built-in potential in p-n junctions. After joining p-type and n-type semiconductors, electrons from the n region near the pn interface tend to diffuse into the p region. As electrons diffuse, they leave positively charged ions (donors) in the n region. Likewise, holes from the p-type region near the pn interface begin to diffuse into the n-type region, leaving fixed ions (acceptors) with negative charge. The regions close to the pn interfaces lose their neutrality and become charged, forming a space charge region or depletion layer. The electric field created by the space charge region opposes the diffusion process for both electrons and holes. There are two concurrent phenomena: the diffusion process, which tends to generate more space charge, and the electric field generated by the space charge, which tends to counteract the diffusion. The two counterbalancing phenomena establish an equilibrium, which forms a potential difference across the

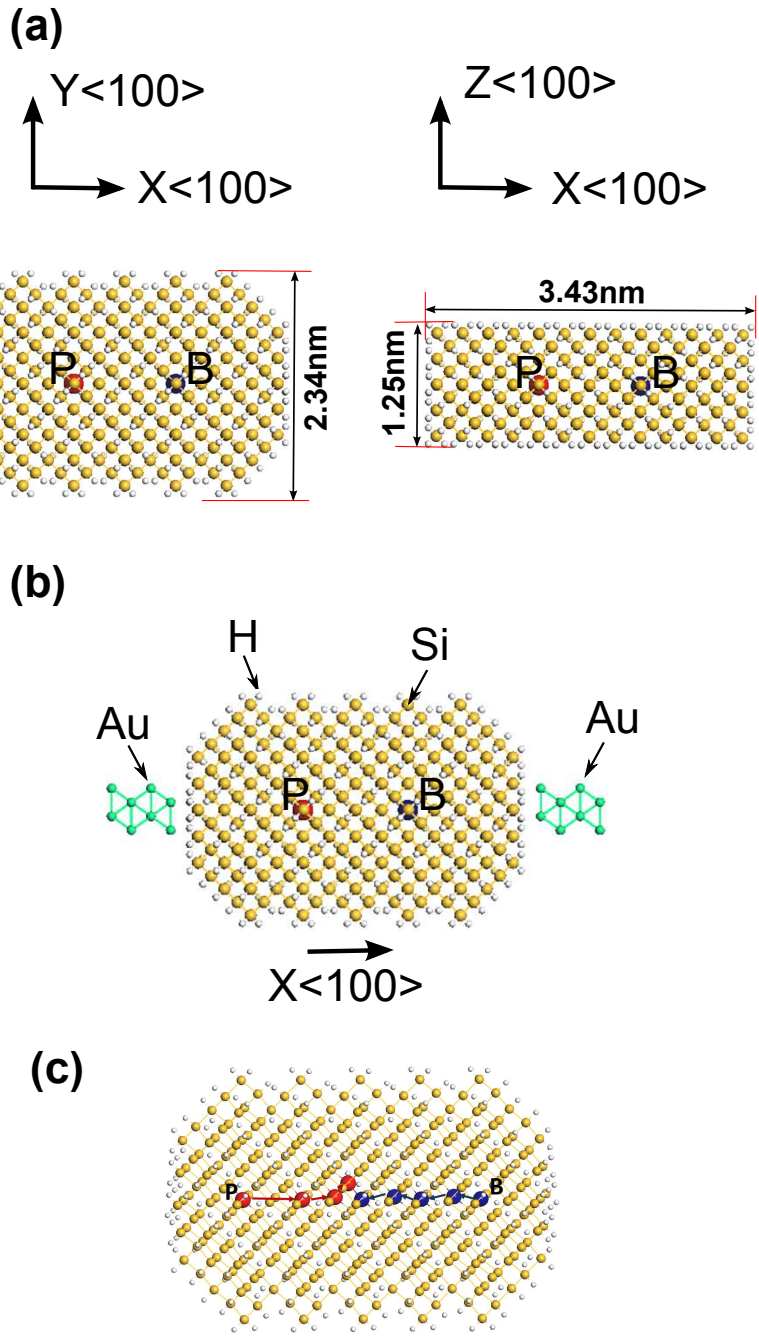

Figure 5.1: (a) The P-B co-doped Si nanorod (P-B SNR) ($Si_{356}PH_{244}$) viewed on the XY and XZ planes, (b) The view of P-B SNR with two Au electrodes on the XZ plane, (c) The positions of the P and B atom when they come closer. The white, yellow, green, red, and blue balls represent H, Si, Au, P, and B atoms, respectively.

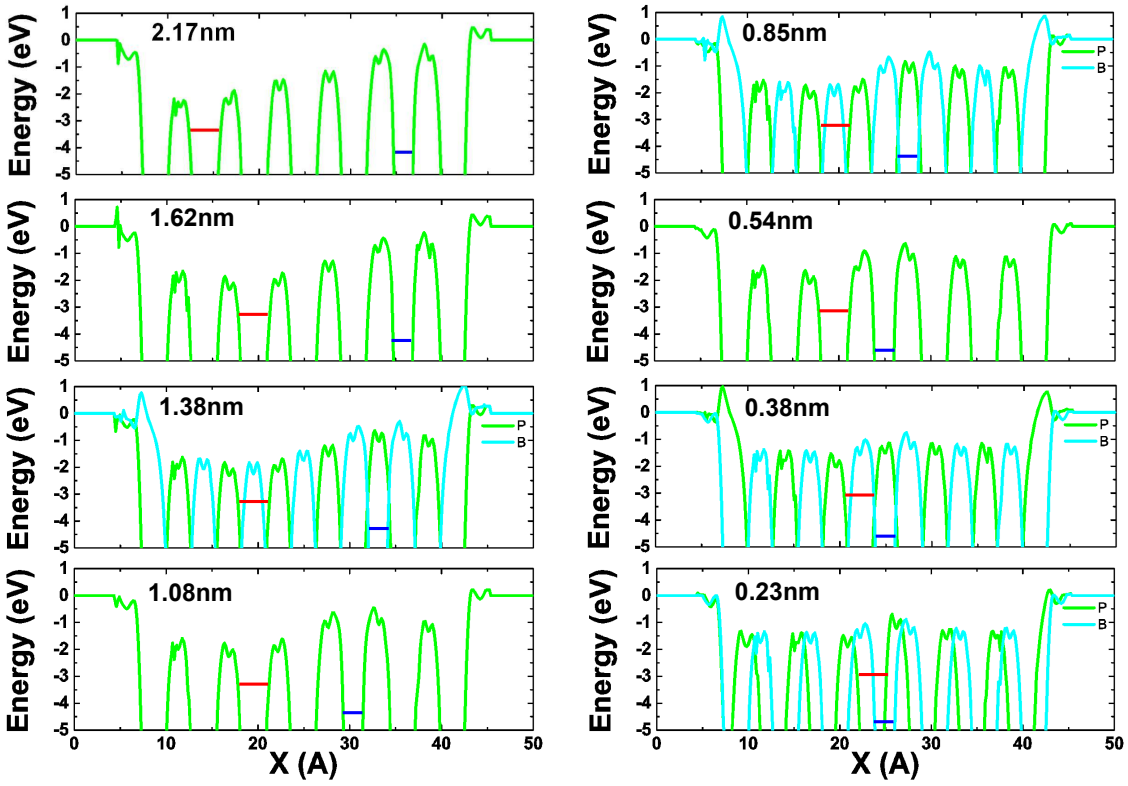

Figure 5.2: The effective atomistic potentials along the X direction, which acrosses the P and B sites. With the distance of 1.38 nm, 0.85 nm, 0.38 nm, and 0.23 nm, the P atom does not locate at the same line with the B atom. The donor energy level (red) and acceptor energy level (blue) are also indicated at the position of the P and B atoms, respectively.

junction. This potential difference is called the built-in potential.

In bulk Si, the D^0 and A^0 are shallow (around 45 meV below and above the conduction and valence bands, respectively). Hence, the electrons and holes can easily diffuse into the opposite sites to form a built-in potential. However, in nano Si of less than 3 nm, the D^0 and $A^0$are deep due to the strong confinement effect. This results in large energy separation of the D^0 and A^0 in nano Si. The atomistis built-in potential strongly depend on the interaction between the donor D^0 and acceptor A^0 ground states.

Figure 5.2 shows the effective atomistic potentials along the X direction, which crosses the P and B sites. The atomistic built-in potential is calculated as the sum of the neutral atom potential and the Hartree potential, which considers the Coulomb electron-electron interactions and can be obtained using the Poisson equation. With distances of 1.38 nm, 0.85 nm, 0.38 nm, and 0.23 nm, the P atom

is not situated on the same line as the B atom. The donor energy level (red) and acceptor energy level (blue) are also indicated at the positions of the P and B atoms, respectively. We can see clearly that the position of the donor energy level is well below the peak effective atomistic potentials near the P site compared with the value of 45 meV in the bulk (¿ 1 eV for the D^0 in the 3nm Si nanorod). The different effective atomistic potentials at the P site and B site are clearly evident, and this difference decreases from about 1.5 eV to around 0.5 eV when two dopants move towards each other from 2.17 nm to 0.23 nm. The decrease in the atomistic built-in potential can be explained by the increase in the D^0 in the 3nm Si nanorod). The different effective atomistic potential at the P site and B site can be easily seen. This difference decreases from about 1.5 eV to around 0.5 eV when two dopants come closer from 2.17 nm to 0.23 nm. The decrease of the atomistic built-in potential can be explained by the increase of the D^0 and A^0 energy separation. When two dopants come closer, the A^0 and D^0states repel each other and become shallower. The increase in the D^0 state leads to an increase in the effective atomistic potential at the phosphorus site, while the decrease in the A^0 state leads to a decrease in the effective atomistic potential at the boron site. As a result, the different atomistic built-in potentials of the phosphorus site and boron sites decrease. In the next section, I will discuss in detail how the D^0 and A^0 interact in nano Si.

5.4 The interaction of donor ground state and acceptor ground state in phosphorus-boron co-doped silicon nanorods

First, I will discuss the donor and acceptor ground state in a P-B co-doped Si nanorod. Figure 5.3 shows the donor and acceptor ground state in a P-B co-doped Si nanorod. The PDOS at P atom is dominated by the s-orbital while the PDOS at the B atom is dominated by the p-orbital. The donor ground state D^0 is therefore non-degenerated with s-like symmetry. The acceptor ground state A^0 is three-fold degenerated with p-like symmetry. The wavefunctions corresponding to the non-degenerated donor ground state D^0 and the three-fold degenerated acceptor ground state A^0 are plotted in Fig. 5.3. According to linear combination atomic orbitals theory, the donor ground state D^0 is combined mainly by s orbitals of P atoms and p orbitals of Si atoms, while the acceptor ground state A^0 is combined mainly by p orbitals of B atoms and p orbitals of Si atoms.

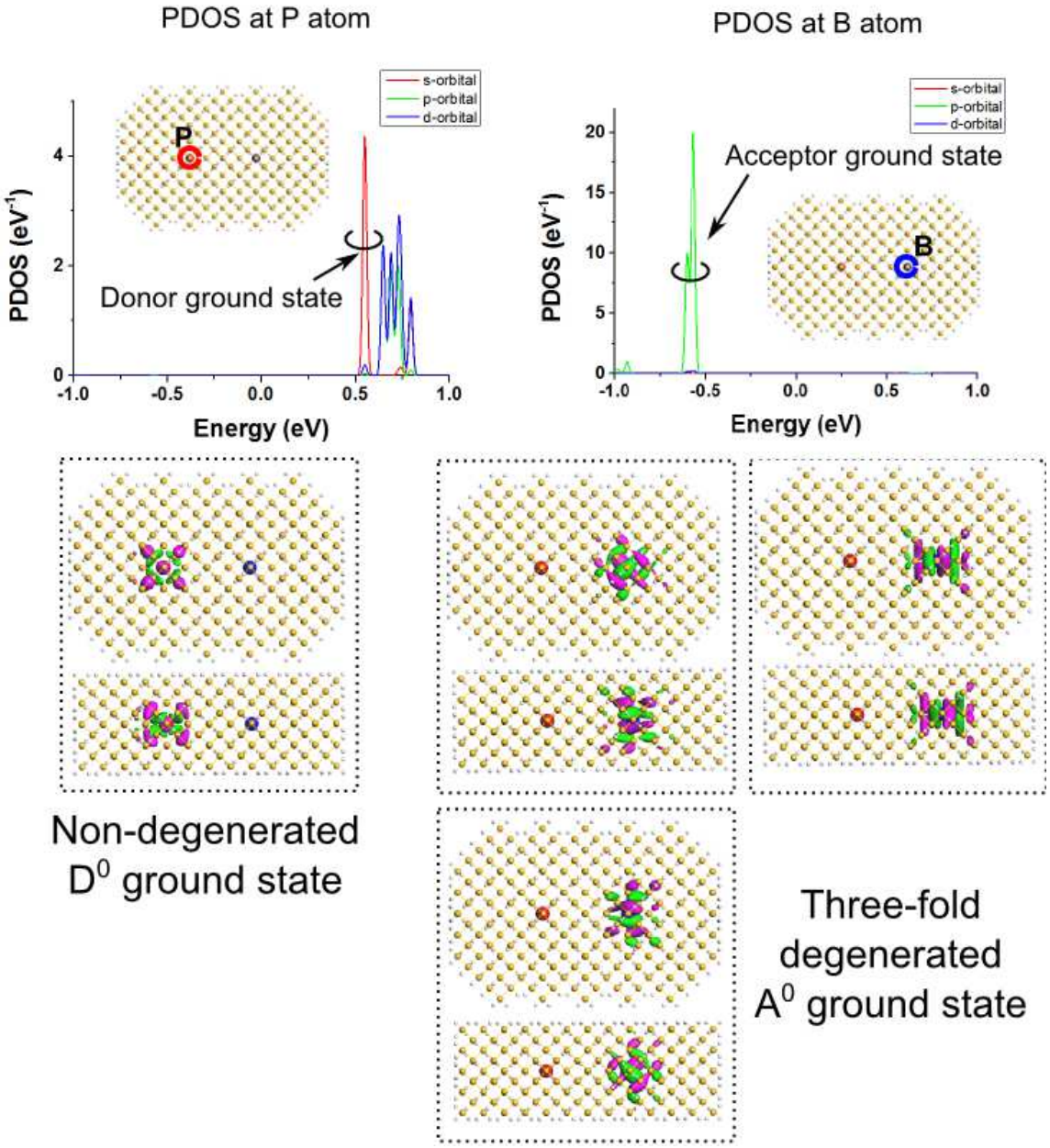

Figure 5.3: The donor and acceptor ground state in a P-B co-doped Si nanorod. The donor ground state D^0 is non-degenerated with s-like symmetry. The acceptor ground state A^0 is three-fold degenerated with p-like symmetry. The wavefunctions were viewed from the top and the side of the Si nanorod.

To study the interaction between the donor D^0 and acceptor A^0 ground states, I changed the P-B seperation in a Si nanorod. Figure 5.4 shows the changes of the PDOS onto P and B atoms and the molecular energy spectra when the distance between two dopants decreases from 2.17 nm to 0.23 nm. The Fermi level was set at 0 eV. The states below 0 eV correspond to the acceptor A^0 ground states and HOMOs (the highest occupied molecular orbitals),, while the density of states above 0 eV correspond to the donor D^0 and LUMOs (the lowest unoccupied molecular orbitals).

When two dopants come closer, the energy gap between the A^0 and D^0 increases, which is similar to the bonding and antibonding behavior in the two-level model.

Figure **??** shows the energy levels of acceptor ground states and donor ground states when the two dopants come closer. The energy gaps between the A^0 and D^0 are plotted as a function of the distance between the two dopants. It is evident that the energy gaps increase when the distance decreases. The increase in the energy gaps results in the acceptor and donor ground states becoming shallower, as indicated in Fig 5.2. Figure 5.6 shows the donor ground state in P-B co-doped Si nanorods with different P-B separations: 2.17, 1.08, 0.38, and 0.23 nm. The wavefunctions were viewed from the top and the side of the Si nanorod. Here, it can be seen that the donor ground state is distorted when the two dopants come closer. Figure 5.7 shows acceptor ground states in P-B co-doped Si nanorods with different P-B separations: 2.17, 1.08, 0.38, and 0.23 nm. Again, the wavefunctions were viewed from the top and the side of the Si nanorod. It can be seen that the acceptor ground state is distorted when the two dopants come closer. Such interactions of the A^0 and D^0an be understood from the point of view of molecular orbital theory. According to molecular orbital (MO) theory, when atomic orbitals interact the resulting molecular orbital can be classified as one of three types: bonding, antibonding, or nonbonding. Here, we focus on bonding and antibonding. Bonding MOs are bonding interactions between atomic orbitals and are constructive (in-phase) interactions, and they are lower in energy than the atomic orbitals that combine to produce them. Antibonding MOs are antibonding interactions between atomic orbitals and are destructive (out-of-phase) interactions, with a nodal plane where the wavefunction of the antibonding orbital is zero between the two interacting atoms. Antibonding MOs are higher in energy than the atomic orbitals that combine to produce them. Figure 5.5 shows the wavefunctions of edge states in single P-doped, pure Si, single B-doped and co-doped P-B. I call the first state

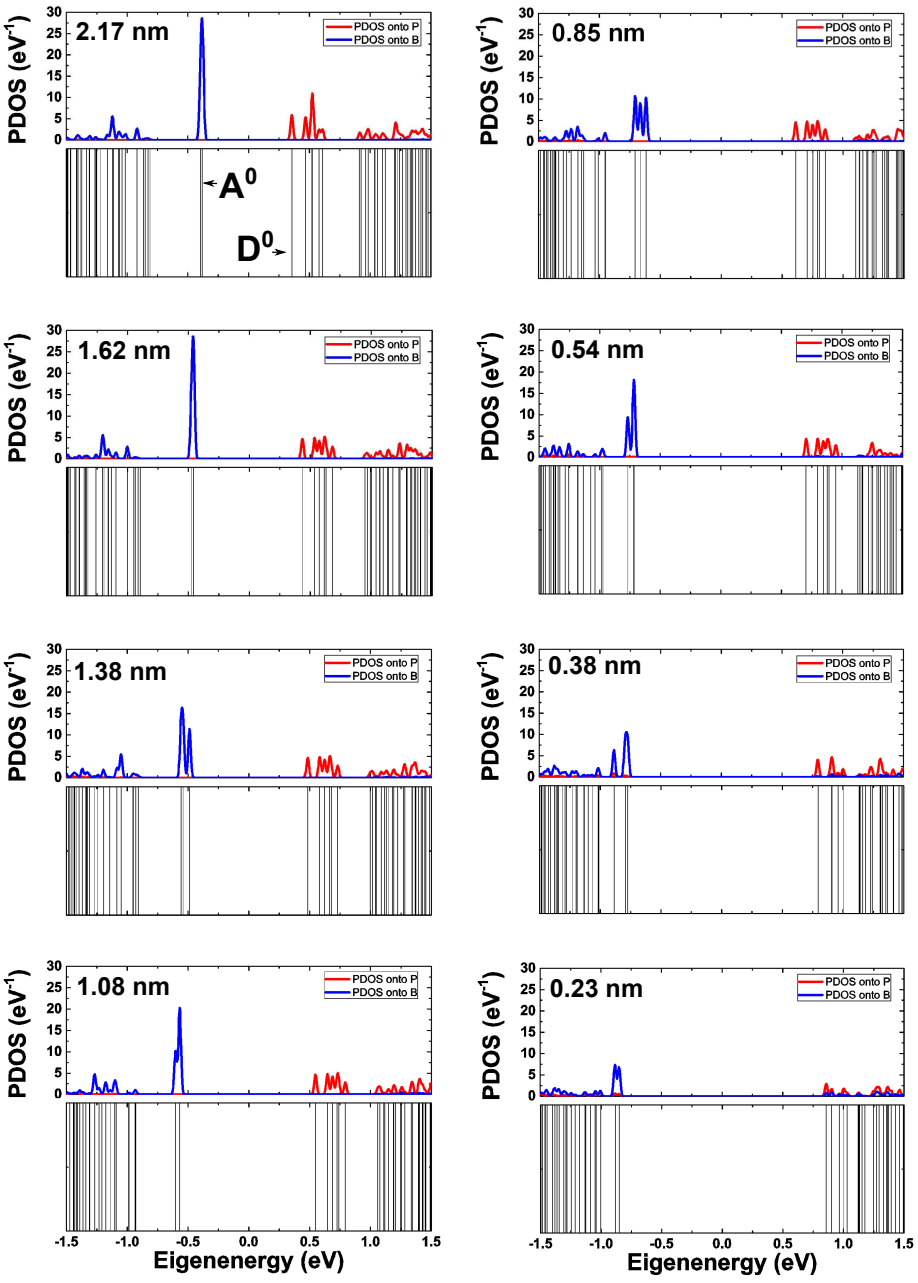

Figure 5.4: The PDOS onto P and B atom and the molecular energy spaectra in Si nanorod when P and B come closer.

below the D^0 is D^{-1}, the first state above A^0 is A^1. Compared to the LUMO state of pure nano Si, the D^0 state is constructive. Compared to the LUMO state of pure nano Si, the A^1 state is destructive. In Fig.5.5, when two dopants P and B are co-doped, the D^0 wavefunction is destructive at the Boron site, the A^0 wavefunction is destructive at the Phosphorus site. The wavefunctions become less localized and shallower.

To study the transport via the A^0 and D^0, I have carried out the transmission spectra calculation as shown in Fig. 5.9. When two dopants come closer, the A^0 and D^0 states move closer to the Si related valence state and the Si related conduction state, respectively. The decrease in the PDOS at A^0 and D^0 also shows that the localization around the dopants of the A^0 and D^0 states decreases. Consistently, the transmission peaks at the D^0 states increase. The transmission at the A^0 is very small compare to the transmission at the D^0 and cannot be seen in 5.9, which is due to the fact that the atomistic effective potential at the B site is deeper than that at the P site. The amplitude of the wavefunction square at the B site is higher than that at the P site, as can be seen in Fig. 5.8. This suggests that the acceptor ground state is more localized than the donor ground state. The transmission via the acceptor ground states is therefore lower than transmission via the donor ground state. Moreover, because the A^0 and D^0 states both become shallower the transmissions associated with dopant induced states change from discrete in nature to continuous.

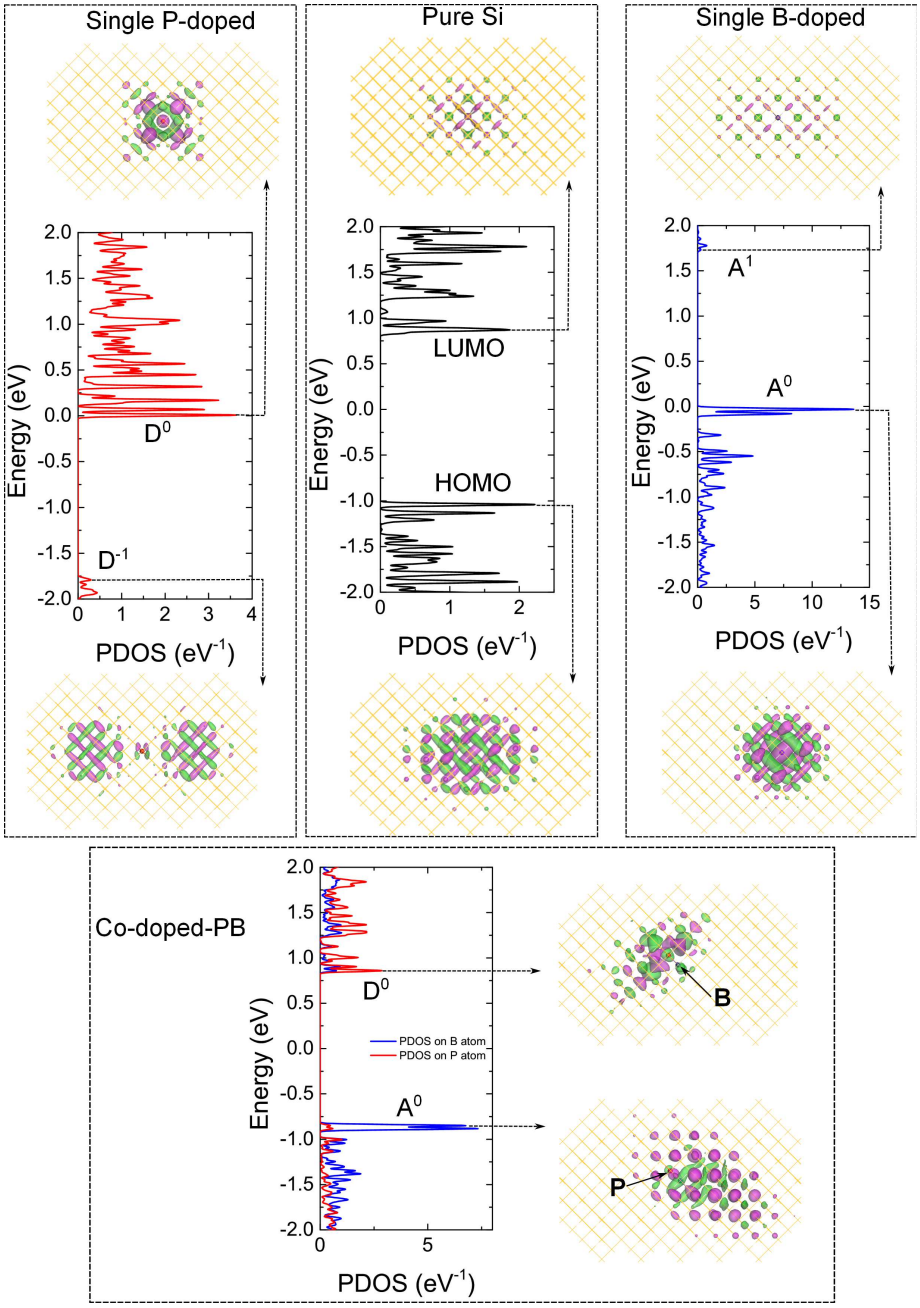

Figure 5.5: The wavefunctions of edge states in single P-doped, pure Si, single B-doped and co-doped P-B.

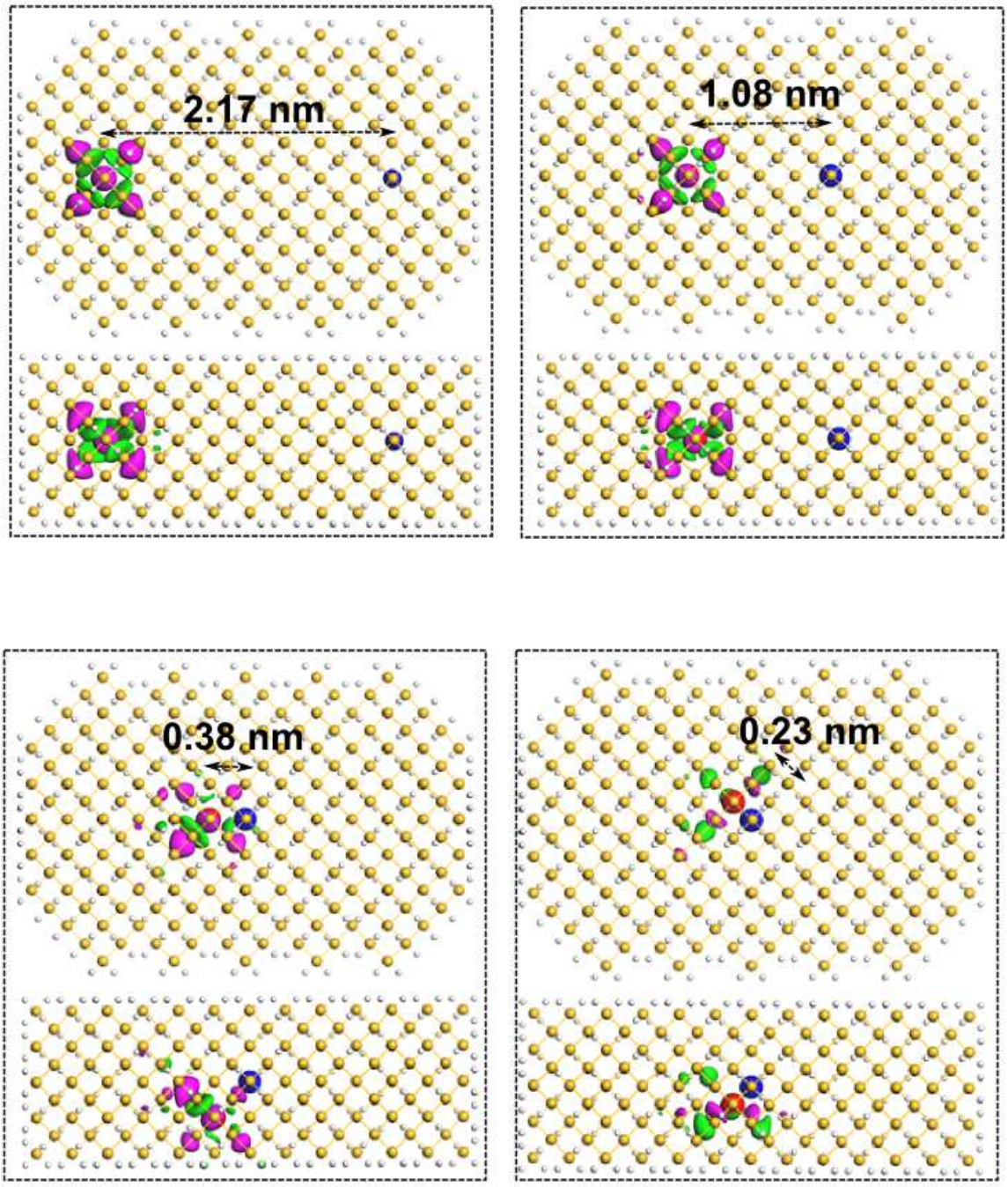

Figure 5.6: The donor ground state in a P-B co-doped Si nanorods with diferent P-B separations: 2.17, 1.08, 0.38, and 0.23 nm. The wavefunctions were viewed from the top and the side of the Si nanorod.

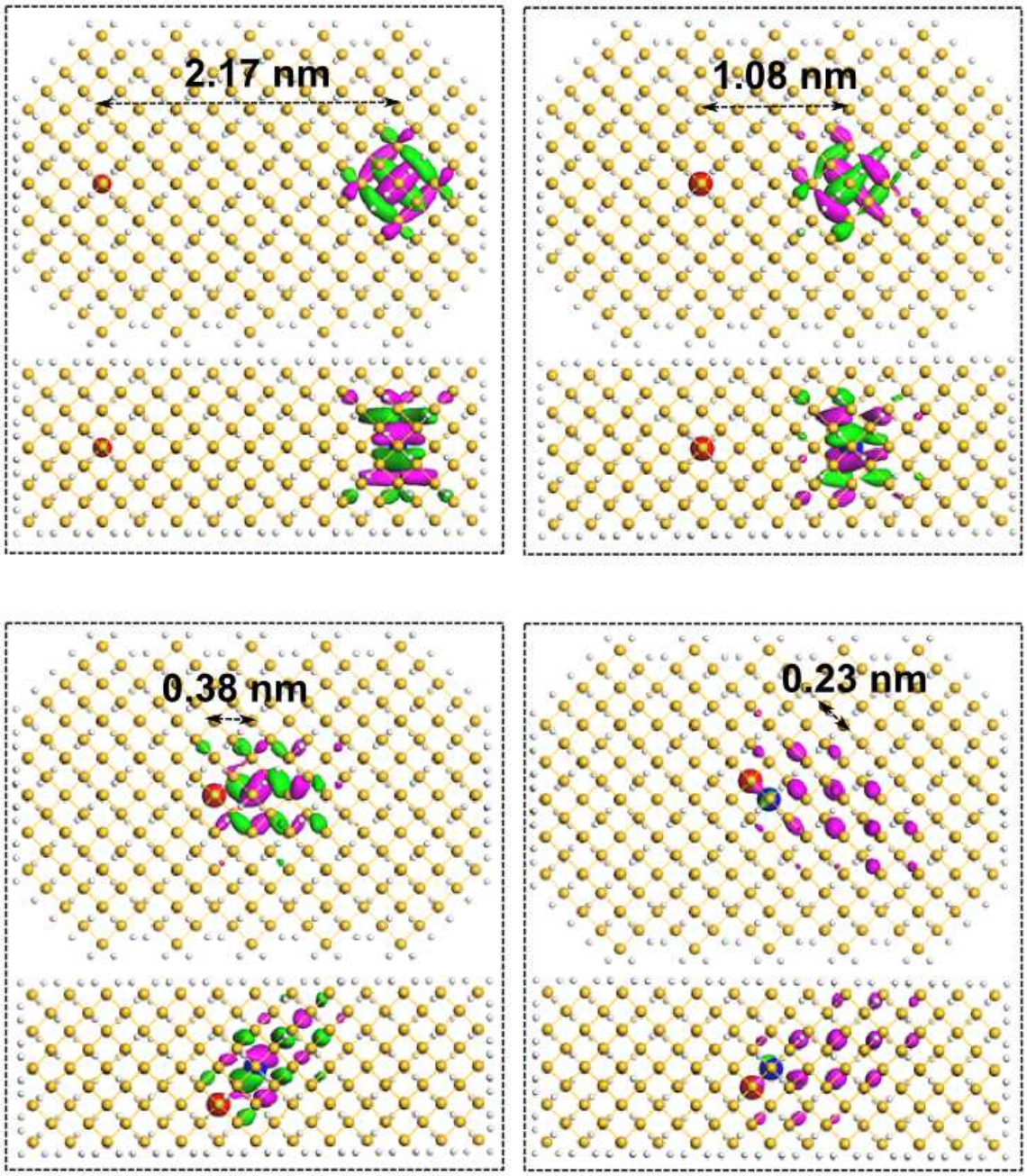

Figure 5.7: The acceptor ground state in a P-B co-doped Si nanorods with diferent P-B separations: 2.17, 1.08, 0.38, and 0.23 nm. The wavefunctions were viewed from the top and the side of the Si nanorod.

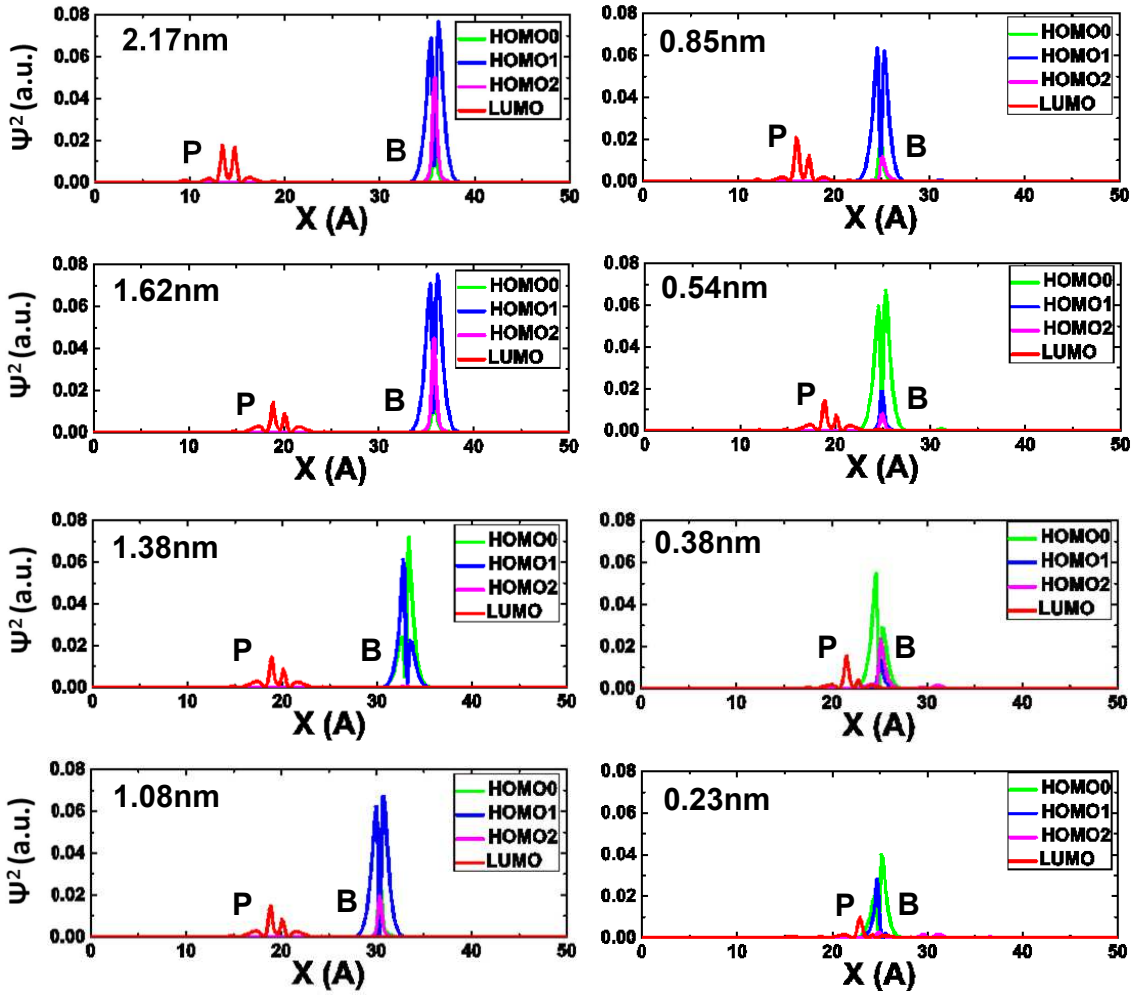

Figure 5.8: The projections of the wavefunction squares of the D^0 and three degenerated A^0 onto the X direction when two dopants come closer.

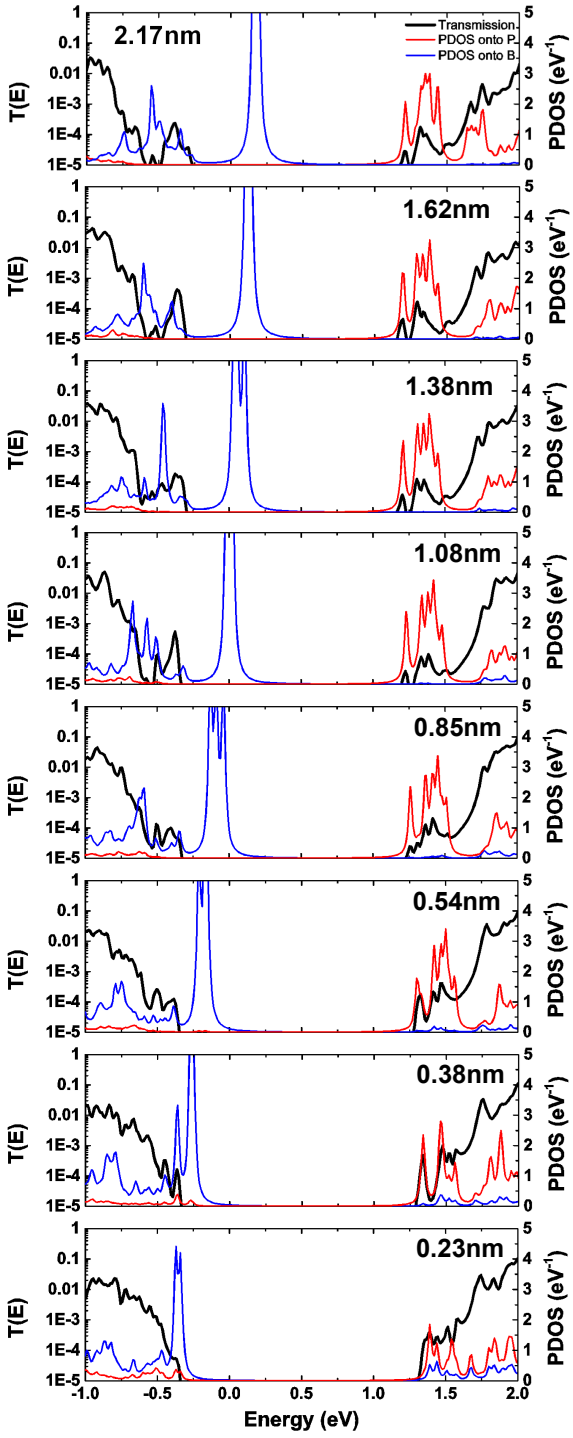

Figure 5.9: The PDOS onto the P and B atom plotted with the transmission sprectra when two dopants come closer.

5.5 Summary

In this chapter, I have conducted first-principles calculations to investigate the electronic and transport properties of P-B co-doped Si nanostructures. When two dopants move closer, the energy gap between the A^0 and D^0increases. This is similar to the antibonding behavior in the two-level model. Furthermore, when two dopants come closer, the donor and acceptor ground state repel each other. The distortions in wavefunctions are due to the destructive interaction of the B and P original atomic orbitals. As a result, the A^0 and D^0 states become less localized and shallower. This is consistent with the transmission analysis that the transmissions associated with dopant induced states change from discrete in nature to continuous.

Chapter 6

Conclusion and future work

6.1 Conclusion

In this thesis, the binding energy of donor electrons in single P-doped Si nanorods was studied theoretically by using DFT and non-equilibrium Green's function method. It has been determined that the hybridization of the phosphorus electron states and the silicon electron states is significant not only at the donor ground state but also at the donor excited states in silicon nanorods. The PDOS-3DWFs analysis has enabled me to clarify the gradually decreasing contribution of the phosphorus electron states from the donor ground states to the higher-energy donor excited states. The first conductive state has been defined as where electrons start to fully transport through the structure. As for the operation of single dopant devices, the isolated current peak at a certain temperature can be considered as the tunneling current via an individual dopant. Thus, the barrier energy required for electron can tunnel via single dopant is especially important. The new definition of the first conductive state was introduced in order to calculate this kind of barrier energy. By using the PDOS-3DWFs analysis, I have been able to identify the first conductive states. Following this, I applied the PDOS-3DWFs method to estimate the binding energy of phosphorus electrons in single P-doped cross-shaped Si models. The results of both the ab-initio calculations and the experimental results of the stub-channel FETs are consistent. For the single P-doped cross-shaped Si models, the PDOS-3DWFs method shows an increase in binding energy when the P atom moves toward the edge. When the P atom is situated at the wing of the cross-shaped model, it is more difficult for the wavefunction to spread entirely within the structure, especially along the horizontal transport direction

compared to cases where the P atom is located at the center. For the stub-channel FETs, the barrier energy attracted from the I_D-$V_G$characteristics shows a higher value for the conventional straight channel transistor. The P atoms are more confined at the edge of the stub-channel transistor compared to the conventional straight channel transistor. The DFT calculation for the positional dependence of the P dopants of the binding energy has therefore produced results that are consistent with the experimental study. Finally, the interaction between the donor ground state and the acceptor ground state was investigated theoretically in P-B co-doped Si nanorods; when the two dopants come closer, the energy gap between the A^0 and D^0increases, which is consistent with the transmission analysis that the transmissions associated with dopant induced states change from discrete in nature to continuous. Moreover, the different effective atomistic potential at the P site and B site decreases from about 1.5 eV to around 0.5 eV when the two dopants move towards each other from 2.17 nm to 0.23 nm. This suggests that the atomistic built-in potential in co-doped silicon nanorods strongly depends on the P-B separation.

I have concluded my study as follows:

- In bulk silicon, the donor ground state is shallow and independent from the bottom of the conduction band of Si crystal. In nano silicon, which has dimensions smaller than the Bohr radius of donor electrons in bulk, the interaction between the donors related states and host Si conduction states becomes significant due to the strong nanoscale confinement. The binding energy in nano Si therefore need to be studied from a different point of view to the binding energy in bulk Si. In past studies, the binding energy of dopant electrons in nano Si has been defined as the difference between the ionization energy calculated for the single P-doped Si nanostructures and the electron affinity calculated for un-doped Si nanostructures. The first conductive state was determined through the electron affinity of the un-doped Si nanostructures. This definition however is similar to the definition for bulk Si and fails to include the strong interaction between phosphorus electrons and silicon, which can be described by the hybridization of the donor electron states and the Si electron states in extremely downscaled Si nanostructures. The PDOS-3DWFs analysis has enabled me to clarify the gradually decreasing contribution of the phosphorus electron states from the donor ground states to the higher-energy donor excited states. I have defined the first conductive

state as where electrons start to be fully transported through the structure. As for the operation of single dopant devices, the isolated current peak at a certain temperature can be considered as the tunneling current via an individual dopant. Therefore, the barrier energy required for electron can tunnel via single dopant is particularly significant. The new definition of the first conductive state is introduced in order to calculate this kind of barrier energy. By using the PDOS-3DWFs analysis, I have been able to identify the first conductive states. (Chapter 3)

- I have calculated the binding energy of donor electrons in the single P-doped Si nanorods, which have a smaller average radius smaller than 1.4 nm as the difference between the first conductive state and the donor ground state. I have found that the binding energy is around 1.5 eV, while the conventional method results in increasing function due to the reduction in the nanorod's radius. The difference is due to the fact that the conventional method does not include the hybridization between the phosphorus electron states and silicon electron states at the first conductive state. As the size decreases below 1.4 nm, the first conductive states are capped near the peak atomistic effective potentials at the P donor sites. This causes the binding energy in small nanorods, which are smaller than 1.4 nm, to be weakly dependant on the size when the size continues to decrease. (Chapter 3)

- This fact signifies a good tolerance of the binding energy, which governs the operating temperature of the single dopant-based transistors in practice. The transmission spectra, which reflects the transportation properties of electrons in the Si nanorod's bandwidth by two electrodes, shows consistent results with the PDOS-3DWFs method and this fact proves the validity of our new method. (Chapter 3)

- I used the PDOS-3DWFs method to estimate the binding energy of phosphorus electrons in single P-doped cross-shaped Si models, concluding that the binding energy increases when the P atom moves from the center toward to the wing of the cross structures while the conventional method results an independent function by changing the P position. The difference is due to the fact that the conventional method does not include the impact of the positional dependence of the P dopant on the energy of the first conductive states. When the P atom is situated at the wing of the cross-shaped structures, it becomes more difficult for the wavefunction to spread entirely within the

structure, especially along the horizontal transport direction compared to cases where the P atom is located at the center. As a result, higher energy is needed for the first fully distributed wavefunction. (Chapter 4)

- The results obtained from the ab-initio calculations are consistent with the experimental results for the stub-channel FETs [13]. For the single P-doped cross-shaped Si models, the PDOS-3DWFs method shows an increase in binding energy when the P atom moves toward the wing. For the experimental stub-channel FETs, the barrier energy extracted from the I_D-V_G characteristics shows a higher value for the stub-channel transistor than for the conventional straight channel transistors, which is due to the fact that the P dopants are more confined at the stub of stub-channel transistor compared to the conventional straight channel transistors. This leads to a deeper donor ground state or higher barrier energy. This suggestion has been confirmed by my simulation of single P-doped cross-shaped Si models. (Chapter 4)

- The D^0 wavefunction is detractive at the boron site whereas the A^0 wavefunction is detractive at the phosphorus site. When the two dopants come closer, the destructive interaction of the B and P original atomic orbital increases. As a result, the wavefunction values of A^0 and D^0 at the boron and phosphorus sites decrease. The wavefunctions become less localized and shallower. This is consistent with the transmission analysis that the transmissions associated to dopant induced states changes from discrete in nature to continuous. (Chapter 5)

6.2 Future work

The dopant-based devices produced from single dopant electronics will establish a new group of extremely-small and low power devices, including single-electron FETs, single electron memory devices, single electron transfer devices, and photonic devices. Furthermore, aiming at room temperature operation of dopant atom devices for practical implementation, a new approach will be proposed such as utilizing the interacting-dopants in the channel. The PDOS-3DWFs analysis can be used to theoretically investigate the interaction between dopants. Moreover, this method is also useful for estimate the binding energy of other donors such as Sb and Bi in nano Si. For photonic devices, tunneling transport via the donor and acceptor ground

states in P-B co-doped Si nanorod models using the DFT-NEGF theory is expected to clarify inter-band tunneling transportation in real nano p-n junctions. Significant progress was made in the first decade of the 21st century and it was demonstrated that the power of a large number of small processors can be utilized to achieve high performance. In 2004, the Earth Simulator supercomputer built by NEC at the Japan Agency for Marine-Earth Science and Technology (JAMSTEC) reached 35.9 teraflops using 640 nodes, each with eight proprietary vector processing chips. In July 2011, the 8.1 peta flop Japanese K computer became the fastest in the world using over 60,000 commercial scalar SPARC64 processors housed in over 600 cabinets. The fact that the K computer is over 60 times faster than the Earth Simulator and that the Earth Simulator is ranked as the 68th fastest system in the world only seven years after holding the top spot demonstrates both the rapid increase in top performance and the widespread growth of supercomputing technology worldwide. This fact encourages scientists to simulate bigger and bigger structures, and the gap between the calculations and experimentation can therefore be filled in near future.

Bibliography

[1] C. Shin and I. J. Park *IEEE Electron Device Lett*, vol. 34, 2013.

[2] C. Shin, N. Damrongplasit, X. Sun, and Liu *IEEE Trans. Electron Devices*, vol. 58, 2011.

[3] C. Shin, M. H. Cho, and Liu *IEEE Trans. Electron Devices*, vol. 57, 2011.

[4] C. Shin, "State-of-the-art silicon device miniaturization technology and its challenges," *IEICE Electronics Express*, vol. 11, no. 10, pp. 20142005–20142005, 2014.

[5] R. H. Dennard, F. H. Gaensslen, V. L. Rideout, and A. R. Leblanc *IEEE J. Solid-State Circuits*, vol. 9, 1971.

[6] K. Bernstein, D. J. Pearson, and N. J. Rohrer *IBM Journal of Research and Development*, vol. 50, 2009.

[7] Y. Yasuda, M. Takamiya, and T. Hiramoto, "Separation of effects of statistical impurity number fluctuations and position distribution on vth fluctuations in scaled mosfets," *Electron Devices, IEEE Transactions on*, vol. 47, pp. 1838–1842, Oct 2000.

[8] A. Asenov, "Random dopant induced threshold voltage lowering and fluctuations in sub-0.1 mu;m mosfet's: A 3-d ldquo;atomistic rdquo; simulation study," *Electron Devices, IEEE Transactions on*, vol. 45, pp. 2505–2513, Dec 1998.

[9] A. Asenov and S. Saini, "Suppression of random dopant-induced threshold voltage fluctuations in sub-0.1- mu;m mosfet's with epitaxial and delta;-doped channels," *Electron Devices, IEEE Transactions on*, vol. 46, pp. 1718–1724, Aug 1999.

[10] G. Tsutsui, M. Saitoh, T. Nagumo, and T. Hiramoto, "Impact of soi thickness fluctuation on threshold voltage variation in ultra-thin body

soi mosfets," *Nanotechnology, IEEE Transactions on*, vol. 4, pp. 369–373, May 2005.

[11] T. Shinada, S. Okamoto, T. Kobayashi, and I. Ohdomari, "Enhancing semiconductor device performance using ordered dopant arrays," *Nature*, vol. 437, p. 4, 7 2005.

[12] M. Fuechsle, J. A. Miwa, S. Mahapatra, H. Ryu, S. Lee, O. Warschkow, L. C. L. Hollenberg, G. Klimeck, and M. Y. Simmons., "A single-atom transistor," *Nature Nanotechnology*, vol. 7, p. 242, 2012.

[13] E. Hamid, D. Moraru, Y. Kuzuya, T. Mizuno, L. T. Anh, H. Mizuta, and M. Tabe, "Electron-tunneling operation of single-donor-atom transistors at elevated temperatures," *Phys. Rev. B*, vol. 87, p. 085420, Feb 2013.

[14] D. Moraru, E. Hamid, Y. Kuzuya, T. Mizuno, L. T. Anh, H. Mizuta, and M. Tabe, "Experimental and ab initio study of donor state deepening in nanoscale soi-mosfets," *Transactions of the Materials Research Society of Japan*, vol. 38, no. 2, pp. 261–264, 2013.

[15] D. V. Averin and K. K. Likharev, "Coulomb blockade of single-electron tunnelling, and coherent oscillations in small tunnel-junctions," *J. Low Temp. Phys.*, vol. 62, 1986.

[16] T. A. Fulton and G. J. Dolan, "Observation of single-electron charging effects in small tunnel junctions," *Phys. Rev. Lett.*, vol. 59, pp. 109–112, Jul 1987.

[17] J. Gorman, D. G. Hasko, and D. A. Williams, "Charge-qubit operation of an isolated double quantum dot," *Phys. Rev. Lett.*, vol. 95, p. 090502, Aug 2005.

[18] Y. Y. Wei, J. Weis, K. v. Klitzing, and K. Eberl, "Single-electron transistor as an electrometer measuring chemical potential variations," *Applied Physics Letters*, vol. 71, no. 17, 1997.

[19] M. W. Keller, J. M. Martinis, N. M. Zimmerman, and A. H. Steinbach, "Accuracy of electron counting using a 7junction electron pump," *Applied Physics Letters*, vol. 69, no. 12, 1996.

[20] P. Lafarge, H. Pothier, E. Williams, D. Esteve, C. Urbina, and M. Devoret, "Direct observation of macroscopic charge quantization," *Zeitschrift fr Physik B Condensed Matter*, vol. 85, no. 3, pp. 327–332, 1991.

[21] A. Fujiwara, Y. Takahashi, K. Murase, and M. Tabe, "Timeresolved measurement of singleelectron tunneling in a si singleelectron transistor with satellite si islands," *Applied Physics Letters*, vol. 67, no. 20, 1995.

[22] R. A. Smith and H. Ahmed, "Gate controlled coulomb blockade effects in the conduction of a silicon quantum wire," *Journal of Applied Physics*, vol. 81, no. 6, 1997.

[23] H. Sellier, G. P. Lansbergen, J. Caro, S. Rogge, N. Collaert, I. Ferain, M. Jurczak, and S. Biesemans, "Transport spectroscopy of a single dopant in a gated silicon nanowire," *Phys. Rev. Lett.*, vol. 97, p. 206805, Nov 2006.

[24] Y. Ono, K. Nishiguchi, A. Fujiwara, H. Yamaguchi, H. Inokawa, and Y. Takahashi, "Conductance modulation by individual acceptors in si nanoscale field-effect transistors," *Applied Physics Letters*, vol. 90, no. 10, pp. –, 2007.

[25] M. A. H. Khalafalla, Y. Ono, K. Nishiguchi, and A. Fujiwara, "Identification of single and coupled acceptors in silicon nano-field-effect transistors," *Applied Physics Letters*, vol. 91, no. 26, pp. –, 2007.

[26] A. S. Martins, R. B. Capaz, and B. Koiller, "Electric-field control and adiabatic evolution of shallow donor impurities in silicon," *Phys. Rev. B*, vol. 69, p. 085320, Feb 2004.

[27] C. J. Wellard and L. C. L. Hollenberg, "Donor electron wave functions for phosphorus in silicon: Beyond effective-mass theory," *Phys. Rev. B*, vol. 72, p. 085202, Aug 2005.

[28] M. J. Calderón, B. Koiller, X. Hu, and S. Das Sarma, "Quantum control of donor electrons at the Si-sio$_2$ interface," *Phys. Rev. Lett.*, vol. 96, p. 096802, Mar 2006.

[29] L. C. L. Hollenberg, A. S. Dzurak, C. Wellard, A. R. Hamilton, D. J. Reilly, G. J. Milburn, and R. G. Clark, "Charge-based quantum computing using single donors in semiconductors," *Phys. Rev. B*, vol. 69, p. 113301, Mar 2004.

[30] D. Moraru, Y. Ono, H. Inokawa, and M. Tabe, "Quantized electron transfer through random multiple tunnel junctions in phosphorus-doped silicon nanowires," *Phys. Rev. B*, vol. 76, p. 075332, Aug 2007.

[31] D. Moraru, M. Ligowski, K. Yokoi, T. Mizuno, and M. Tabe, "Single-electron transfer by inter-dopant coupling tuning in doped nanowire

silicon-on-insulator field-effect transistors," *Applied Physics Express*, vol. 2, no. 7, p. 071201, 2009.

[32] K. Yokoi, D. Moraru, M. Ligowski, and M. Tabe, "Single-gated single-electron transfer in nonuniform arrays of quantum dots," *Japanese Journal of Applied Physics*, vol. 48, no. 2R, p. 024503, 2009.

[33] Z. A. Burhanudin, R. Nuryadi, and M. Tabe, "Detection of field-induced single-acceptor ionization in si by single-hole-tunneling transistor," *Applied Physics Letters*, vol. 91, no. 4, pp. –, 2007.

[34] S. R. Schofield, N. J. Curson, M. Y. Simmons, F. J. Rueß, T. Hallam, L. Oberbeck, and R. G. Clark, "Atomically precise placement of single dopants in si," *Phys. Rev. Lett.*, vol. 91, p. 136104, Sep 2003.

[35] M. Nishizawa, L. Bolotov, and T. Kanayama, "Simultaneous measurement of potential and dopant atom distributions on wet-prepared si(111):h surfaces by scanning tunneling microscopy," *Applied Physics Letters*, vol. 90, no. 12, pp. –, 2007.

[36] M. Ligowski, D. Moraru, M. Anwar, T. Mizuno, R. Jablonski, and M. Tabe, "Observation of individual dopants in a thin silicon layer by low temperature kelvin probe force microscope," *Applied Physics Letters*, vol. 93, no. 14, pp. –, 2008.

[37] M. Tabe, D. Moraru, M. Ligowski, M. Anwar, R. Jablonski, Y. Ono, and T. Mizuno, "Single-electron transport through single dopants in a dopant-rich environment," *Phys. Rev. Lett.*, vol. 105, p. 016803, Jul 2010.

[38] D. Moraru, K. Yokoi, R. Nakamura, T. Mizuno, and M. Tabe, "Tunable single-electron turnstile using discrete dopants in nanoscale soi-fets," *Key Engineering Materials*, vol. 470, pp. 27–32, 2011.

[39] D. Moraru, E. Hamid, J. C. Tarido, S. Miki, T. Mizuno, and M. Tabe, "Memory effects based on dopant atoms in nano-fets," *Advanced Materials Research*, vol. 222, pp. 122–125, 2011.

[40] D. Moraru, A. Udhiarto, M. Anwar, R. Nowak, R. Jablonski, E. Hamid, J. Tarido, T. Mizuno, and M. Tabe, "Atom devices based on single dopants in silicon nanostructures," *Nanoscale Research Letters*, vol. 6, no. 1, 2011.

[41] M. Tabe, A. Udhiarto, D. Moraru, and T. Mizuno, "Single-photon detection by si single-electron fets," *physica status solidi (a)*, vol. 208, no. 3, pp. 646–651, 2011.

[42] D. Moraru, S. Purwiyanti, R. Nowak, T. Mizuno, A. Uharto, D. H, R. J, and M. Tabe, "Individuality of dopants in silicon nano-pn junctions," *Materials Science*, vol. 20, no. 2, 2014.

[43] Kohanoff, *Electroic Structure Calculations for Solides and Solecules*. Cambridge, 2006.

[44] P. Hohenberg and W. Kohn, "Inhomogeneous electron gas," *Phys. Rev.*, vol. 136, pp. B864–B871, Nov 1964.

[45] W. Kohn and L. J. Sham, "Self-consistent equations including exchange and correlation effects," *Phys. Rev.*, vol. 140, pp. A1133–A1138, Nov 1965.

[46] N. S. Wingreen, A.-P. Jauho, and Y. Meir, "Time-dependent transport through a mesoscopic structure," *Phys. Rev. B*, vol. 48, pp. 8487–8490, Sep 1993.

[47] S. Datta, *Electroic Transport in Mesoscopic systems*. Cambridge, 1995.

[48] G. B. Bachelet, D. R. Hamann, and M. Schlüter, "Pseudopotentials that work: From h to pu," *Phys. Rev. B*, vol. 26, pp. 4199–4228, Oct 1982.

[49] N. Troullier and J. L. Martins, "Efficient pseudopotentials for plane-wave calculations," *Phys. Rev. B*, vol. 43, pp. 1993–2006, Jan 1991.

[50] L. Kleinman and D. M. Bylander, "Efficacious form for model pseudopotentials," *Phys. Rev. Lett.*, vol. 48, pp. 1425–1428, May 1982.

[51] P. E. Blöchl, "Generalized separable potentials for electronic-structure calculations," *Phys. Rev. B*, vol. 41, pp. 5414–5416, Mar 1990.

[52] I. Morrison, D. M. Bylander, and L. Kleinman, "Nonlocal hermitian norm-conserving vanderbilt pseudopotential," *Phys. Rev. B*, vol. 47, pp. 6728–6731, Mar 1993.

[53] T. Ozaki and H. Kino, "Numerical atomic basis orbitals from h to kr," *Phys. Rev. B*, vol. 69, p. 195113, May 2004.

[54] J. P. Perdew, K. Burke, and M. Ernzerhof, "Generalized gradient approximation made simple," *Phys. Rev. Lett.*, vol. 77, pp. 3865–3868, Oct 1996.

[55] T. Ozaki, K. Nishio, and H. Kino, "Efficient implementation of the nonequilibrium green function method for electronic transport calculations," *Phys. Rev. B*, vol. 81, p. 035116, Jan 2010.

[56] D. V. Melnikov and J. R. Chelikowsky, "Quantum confinement in phosphorus-doped silicon nanocrystals," *Phys. Rev. Lett.*, vol. 92, p. 046802, Jan 2004.

[57] M. Diarra, Y.-M. Niquet, C. Delerue, and G. Allan, "Ionization energy of donor and acceptor impurities in semiconductor nanowires: Importance of dielectric confinement," *Phys. Rev. B*, vol. 75, p. 045301, Jan 2007.

[58] R. Rurali, B. Aradi, T. Frauenheim, and A. Gali, "Donor levels in si nanowires determined by hybrid-functional calculations," *Phys. Rev. B*, vol. 79, p. 115303, Mar 2009.

[59] G. Cantele, E. Degoli, E. Luppi, R. Magri, D. Ninno, G. Iadonisi, and S. Ossicini, "First-principles study of *n*- and *p*-doped silicon nanoclusters," *Phys. Rev. B*, vol. 72, p. 113303, Sep 2005.

[60] Z. Zhou, M. L. Steigerwald, R. A. Friesner, L. Brus, and M. S. Hybertsen, "Structural and chemical trends in doped silicon nanocrystals: First-principles calculations," *Phys. Rev. B*, vol. 71, p. 245308, Jun 2005.

[61] D. V. Melnikov and J. R. Chelikowsky, "Electron affinities and ionization energies in si and ge nanocrystals," *Phys. Rev. B*, vol. 69, p. 113305, Mar 2004.

[62] Y. M. Niquet, C. Delerue, G. Allan, and M. Lannoo, "Method for tight-binding parametrization: Application to silicon nanostructures," *Phys. Rev. B*, vol. 62, pp. 5109–5116, Aug 2000.

[63] V. A. Belyakov and V. A. Burdov, "Chemical-shift enhancement for strongly confined electrons in silicon nanocrystals," *Physics Letters A*, vol. 367, no. 12, pp. 128 – 134, 2007.

[64] T. Ozaki and H. Kino, "Efficient projector expansion for the ab initio lcao method," *Phys. Rev. B*, vol. 72, p. 045121, Jul 2005.

[65] P. Parida, E. A. Basheer, and S. K. Pati, "Cyclopentadienyl-benzene based sandwich molecular wires showing efficient spin filtering, negative differential resistance, and pressure induced electronic transitions," *J. Mater. Chem.*, vol. 22, pp. 14916–14924, 2012.

[66] P. Andrei and I. Mayergoyz, "Random doping-induced fluctuations of subthreshold characteristics in {MOSFET} devices," *Solid-State Electronics*, vol. 47, no. 11, pp. 2055 – 2061, 2003.

[67] G. P. Lansbergen, R. Rahman, C. J. Wellard, J. C. I. Woo, N. Collaert, S. Biesemans, G. Klimeck, L. C. L. Hollenberg, and S. Rogge., "Gate-induced quantum-confinement transition of a single dopant atom in a silicon finfet," *Nature Physics*, vol. 4, p. 656, 2008.

[68] K. Y. Tan, K. W. Chan, M. Mottonen, A. Morello, C. Yang, J. v. Donkelaar, A. Alves, J.-M. Pirkkalainen, D. N. Jamieson, R. G. Clark, and A. S. Dzurak, "Transport spectroscopy of single phosphorus donors in a silicon nanoscale transistor," *Nano Letters*, vol. 10, no. 1, pp. 11–15, 2010. PMID: 19950969.

[69] E. Prati, M. Belli, S. Cocco, G. Petretto, and M. Fanciulli, "Adiabatic charge control in a single donor atom transistor," *Applied Physics Letters*, vol. 98, no. 5, pp. –, 2011.

[70] Y. Ono, K. Nishiguchi, A. Fujiwara, H. Yamaguchi, H. Inokawa, and Y. Takahashi, "Conductance modulation by individual acceptors in si nanoscale field-effect transistors," *Applied Physics Letters*, vol. 90, no. 10, pp. –, 2007.

[71] F. Iori, E. Degoli, R. Magri, I. Marri, G. Cantele, D. Ninno, F. Trani, O. Pulci, and S. Ossicini, "Engineering silicon nanocrystals: Theoretical study of the effect of codoping with boron and phosphorus," *Phys. Rev. B*, vol. 76, p. 085302, Aug 2007.

[72] F. Iori and S. Ossicini, "Effects of simultaneous doping with boron and phosphorous on the structural, electronic and optical properties of silicon nanostructures," *Physica E: Low-dimensional Systems and Nanostructures*, vol. 41, no. 6, pp. 939 – 946, 2009. Proceedings of the E-MRS 2008 Symposium C: Frontiers in Silicon-Based Photonics.

[73] Y. Ma, X. Chen, X. Pi, and D. Yang, "Lightly boron and phosphorus co-doped silicon nanocrystals," *Journal of Nanoparticle Research*, vol. 14, no. 4, 2012.

[74] A. Udhiarto, D. Moraru, S. Purwiyanti, Y. Kuzuya, T. Mizuno, H. Mizuta, and M. Tabe, "Photon-induced random telegraph signal due to potential fluctuation of a single donoracceptor pair in nanoscale si pn junctions," *Applied Physics Express*, vol. 5, no. 11, p. 112201, 2012.

[75] C. Yang, C. J. Barrelet, F. Capasso, and C. M. Lieber, "Single p-type/intrinsic/n-type silicon nanowires as nanoscale avalanche pho-

todetectors," *Nano Letters*, vol. 6, no. 12, pp. 2929–2934, 2006. PMID: 17163733.

[76] S. ichi Saito, D. Hisamoto, H. Shimizu, H. Hamamura, R. Tsuchiya, Y. Matsui, T. Mine, T. Arai, N. Sugii, K. Torii, S. Kimura, and T. Onai, "Electro-luminescence from ultra-thin silicon," *Japanese Journal of Applied Physics*, vol. 45, no. 7L, p. L679, 2006.

[77] M. Fujii, Y. Yamaguchi, Y. Takase, K. Ninomiya, and S. Hayashi, "Photoluminescence from impurity codoped and compensated si nanocrystals," *Applied Physics Letters*, vol. 87, no. 21, pp. –, 2005.

[78] M. Fujii, K. Toshikiyo, Y. Takase, Y. Yamaguchi, and S. Hayashi, "Below bulk-band-gap photoluminescence at room temperature from heavily p- and b-doped si nanocrystals," *Journal of Applied Physics*, vol. 94, no. 3, 2003.

[79] M. Fujii, Y. Yamaguchi, Y. Takase, K. Ninomiya, and S. Hayashi, "Control of photoluminescence properties of si nanocrystals by simultaneously doping n- and p-type impurities," *Applied Physics Letters*, vol. 85, no. 7, 2004.

[80] S. Purwiyanti, R. Nowak, D. Moraru, T. Mizuno, D. Hartanto, R. Jablonski, and M. Tabe, "Dopant-induced random telegraph signal in nanoscale lateral silicon pn diodes at low temperatures," *Applied Physics Letters*, vol. 103, no. 24, pp. –, 2013.

Publications

Refereed journal papers

[1] Le The Anh, Daniel Moraru, Muruganathan Manoharan, Michiharu Tabe, and Hiroshi Mizuta, *"The impacts of electronic state hybridization on the binding energy of single phosphorus donor electrons in extremely down-scaled silicon nanostructures,"* Journal of Applied Physics, **116** (6), 063705 (2014) [9 page].

[2] Earfan Hamid, Daniel Moraru, Youhei Kuzuya, Takeshi Mizuno, Le The Anh, Hiroshi Mizuta, and Michiharu Tabe, *"Electron-tunneling operation of single-donor-atom transistors at elevated temperatures,"* Physical Review B **87**, 085420 (2013) [5 pages].

[3] Daniel Moraru, Arup Samanta, Le The Anh, Takeshi Mizuno, Hiroshi Mizuta, and Michiharu Tabe *"Transport spectroscopy of coupled donors in silicon nano-transistors"*, Scientific Reports vol. **4**, pp. 06219-1-6 (2014).

[4] Michiharu Tabe, Daniel Moraru, Earfan Hamid, Arup Samanta, Le The Anh, Takeshi Mizuno, and Hiroshi Mizuta, invited talk, *"Dopant-Atom-Based Tunnel SOI-MOSFETs,"* ECS Transactions, vol. **58**, pp. 89-95 (2013).

[5] D. Moraru, E. Hamid, Y. Kuzuya, T. Mizuno, L. T. Anh, H. Mizuta, and M. Tabe, *"Experimental and ab initio study of donor state deepening in nanoscale SOI-MOSFETs,"* Transactions of the Materials Research Society of Japan, vol.**38**, no.2, pp.261-264 (2013).

[6] Le The Anh, Daniel Moraru, Muruganathan Manoharan, Michiharu Tabe, and Hiroshi Mizuta, *"The interaction of the donor-acceptor ground states and its impact on the electronic and transport properties of phosphorus and boron co-doped silicon nanostructures,"* in preparation for submission.

Refereed international conferences

[7] Michiharu Tabe, Daniel Moraru, Earfan Hamid, Arup Samanta, Le The Anh, Takeshi Mizuno, and Hiroshi Mizuta, invited talk, *"Dopant atom devices based on Si nanostructures,"* International WorkShop on New Group IV Semiconductor Nanoelectronics, Sendai, Japan 2014.

[8] D. Moraru, A. Samanta, T. Tsutaya, T. Mizuno, Y. Takasu, L. T. Anh, M. Manoharan, H. Mizuta, and M. Tabe, *"Control of Electron Transport Regimes via Single- and Multiple-Donors in Nano-Channel SOI-FETs,"* Silicon Nanoelectronics Workshop (SNW), Hawaii, USA 2014.

[9] S. Purwiyanti, H. N. Tan, D. Moraru, D. Hartanto, L. T. Anh, M. Manoharan, T. Mizuno, H. Mizuta, and M. Tabe, *"Study of Quantized-Energy Effects in Si Nanoscale Lateral pn Junction Diodes,"* Silicon Nanoelectronics Workshop (SNW), Hawaii, USA 2014.

[10] H. N. Tan, S. Purwiyanti, D. Moraru, L. T. Anh, M. Manoharan, T. Mizuno, H. Mizuta, D. Hartanto, and M. Tabe, *"Impact of Dopant-Induced States on Interband Tunneling in Nanoscale pn Junctions,"* International Conference on Solid State Devices and Materials (SSDM2014), Tsukuba, Japan, 2014.

[11] Arup Samanta, Daniel Moraru, Yohei Kuzuya, K Tyszka, Takeshi Mizuno, Le The Anh, Hiroshi Mizuta, and Michiharu Tabe, *" Dopant-Atom-based SOI-Transistors by Selective Nanoscale Doping,"* International Conference on Solid State Devices and Materials (SSDM2013), Fukuoka, Japan, 2013.

[12] Le The Anh, Daniel Moraru, Takeshi Mizuno, Manoharan Muruganathan, Michiharu Tabe, and Hiroshi Mizuta, *"First-principle analysis of electronic*

states strongly bound to a single Phosphorus donor in Silicon cross-shaped nanostructures, conference paper,", conference proceedings, pp.555-557, The 4^{th} International Worshop on Nanotechnology and Application, Vung Tau, Vietnam 2013.

[13] Le The Anh, Yohei Kuzuya, Daniel Moraru, Takeshi Mizuno, Manoharan Muruganathan, Michiharu Tabe, and Hiroshi Mizuta, *" Ab initio study of Phosphorus donor states in single dopant transistor with a stub-shaped channel,"* Conference on Computational Physics, Kobe, Japan 2012.

Domestic conferences

[14] Le The Anh, Arup Samanta, Daniel Moraru, Takeshi Mizuno, Manoharan Muruganathan, Michiharu Tabe, and Hiroshi Mizuta, *" Ab-initio study of interactive-donor states ofmultiple P-atoms in Si nanoplates,"* The 74^{th} JSAP Autumn Meeting, Doshisha University, Japan 2013.

[15] Arup Samanta, Daniel Moraru, Efran Hamid, Yohei Kuzuya, L. T. Anh, Takeshi Mizuno, Hiroshi Mizuta and Michiharu Tabe, *" Transport Spectroscopy of Dopant States in Randomly-Doped Single-Electron Transistors."* The 74^{th} JSAP Autumn Meeting, Doshisha University, Japan 2013.

[16] Daniel Moraru, Arup Samanta, Le The Anh, Takeshi Mizuno, Hiroshi Mizuta, and Michiharu Tabe, *" Transport via dopant-quantum-dots fabricated by thermal diffusion through nano-masks."* The 74^{th} JSAP Autumn Meeting, Doshisha University, Japan 2013.

[17] Le The Anh, Yohei Kuzuya, Daniel Moraru, Takeshi Mizuno, Manoharan Muruganathan, Michiharu Tabe, and Hiroshi Mizuta, *" Ab initio study of binding energy for single phosphorus donor in silicon nano stub-shaped channel"*, The 60^{th} JSAP Spring Meeting, Kanagawa Institute of Technology, Japan 2013.

[18] Le The Anh, Yohei Kuzuya, Daniel Moraru, Michiharu Tabe, and Hiroshi Mizuta, *" Ab initio study of Phosphorus donor in Si nano-structures: Wave function analysis of P-doped Si nano-disk,"*, The 73rd JSAP Autumn Meeting, Ehime University, Japan 2012.

[19] Earfan Hamid, Daniel Moraru, Yohei Kuzuya, Takeshi Mizuno, Le The Anh, Hiroshi Mizuta, and Michiharu Tabe, *" Energy ionization enhancement and high Temperature operation of single-Dopant Transistors"*, The 73rd JSAP Autumn Meeting, Ehime University, Japan 2012.

[20] Le The Anh, Yohei Kuzuya, Daniel Moraru, Takeshi Mizuno, Manoharan Muruganathan, Michiharu Tabe, and Hiroshi Mizuta, *" First-principle calculations of energy states of a single phosphorus donor atom in silicon stub transistors,"* Annual Meeting of Hokuriku Branch of Japan Physical Society, Kanazawa University, Japan 2012.

Electron tunneling via many-donor quantum dots in nano channel SOI-FETs: Low-temperature I_D-V_G measurements

This experimental minor project was conducted jointly with Doctor Daniel Moraru and Mr. Tsutaya, under the supervision of Professor Michiharu Tabe from Research Institute of Electronics, Shizuoka University. In this project, I measure the I_D-V_G characteristics of selectively P-doped SOI-FETs at low temperature (below 20 K) to observe the electron tunneling via deep donor-induced electronic states of the clusters formed by many P donors in the selective region. It is found that with the regular small positive V_D (5 mV) and small negative V_G (-1 V), the cluster P donors may not be fully ionized. Therefore, the initialization test is done to fully deplete electrons from clusters. The comparisons of the I_D-V_G characteristics before and after the initialization show that the spectra are red-shifted and new features emerge after the initialization. The emerging of new features, which correspond to the tunneling via deeper donor-induced electronic states of the clusters, proves that the initializations effectively deplete electrons from cluster P donors.